Ore Geology Reviews 86 (2017) 1–20

Contents lists available at ScienceDirect

Ore Geology Reviews

journal homepage: www.elsevier.com/locate/oregeo

Formation of the Jinshandian Fe skarn ore field in the Edong district, Eastern China: Constraints from U–Pb and $^{40}Ar/^{39}Ar$ geochronology

Qiaoqiao Zhu [a], Guiqing Xie [a,*], Jingwen Mao [a], Kejun Hou [a], Jinfeng Sun [b], Zongsheng Jiang [a]

[a] MLR Key Laboratory of Metallogeny and Mineral Assessment, Institute of Mineral Resources, CAGS, Beijing 100037, People's Republic of China
[b] Faculty of Earth Sciences, University of Chinese Academy of Sciences, Beijing 100049, People's Republic of China

ARTICLE INFO

Article history:
Received 11 August 2016
Received in revised form 26 January 2017
Accepted 30 January 2017
Available online 3 February 2017

Keywords:
Fe skarn
Jinshandian
Edong district
Magmatic-hydrothermal event
U–Pb geochronology
$^{40}Ar/^{39}Ar$ geochronology

ABSTRACT

The Jinshandian ore field represents one of the largest concentrations of Fe skarn deposits in the Edong district of Eastern China. Orebodies of these deposits occur in skarn along the contacts between quartz diorite or quartz monzonite and Triassic sedimentary country rocks. In this paper, we present new U–Pb geochronological data for magmatic zircon and hydrothermal titanite, as well as $^{40}Ar/^{39}Ar$ ages on hydrothermal phlogopite, to determine whether multiple magmatic-hydrothermal events associated with formation of the Fe skarn deposits in the Jinshandian ore field. The robust U–Pb zircon ages demonstrate that the quartz monzonite and quartz diorite were emplaced at 130 Ma and 127 Ma, receptively. The U–Pb and $^{40}Ar/^{39}Ar$ ages of hydrothermal titanite and phlogopite form the skarn indicate that Fe mineralization also formed at ca. 131–128 Ma, but with an additional 118 Ma hydrothermal event recorded by phlogopite. This geochronology confirms a causative linkage between granitic intrusion and skarn mineralization. The data also indicate that at least two hydrothermal events took place in the Jinshandian ore field, one at 131–128 Ma and the other at ~118 Ma. Integrating these ages from the ore field with previous geochronological data from the broader Edong district, two regional magmatic-hydrothermal events are recognized in the Edong district after 135 Ma, with the older one at 131–127 Ma in excellent agreement with the ~131 Ma formation age of magnetite-apatite deposits in the eastern part of Middle–Lower Yangtze River region, and the younger one at 122–118 Ma post-dating emplacement of the ca. 126 Ma A-type granite and syenite in the eastern part of Middle–Lower Yangtze River region. A detailed comparison between the Fe skarn deposits and magnetite-apatite deposits in the Middle–Lower Yangtze River region suggests that these two deposit types not only share similar alteration assemblages and association with the evaporites within the ore-forming systems, but also may have formed during the same Early Cretaceous magmatic-hydrothermal event.

1. Introduction

Determining the timing of magmatic-hydrothermal events that are related to economic mineral deposit formation is of primary importance to the understanding of ore genesis processes and for developing exploration models. Field observations and isotopic dating have shown that some magmatic-hydrothermal mineral deposits formed from multiple intrusive events (Stein and Cathles, 1997; Maksaev et al., 2004; Cannell et al., 2005; Sillitoe and Mortensen, 2010; Von Quadt et al., 2011; Braxton et al., 2012; Chiaradia et al., 2013; Deckart et al., 2014; Chelle-Michou et al., 2015). Whether or not a specific ore district had experienced multiple mineralization events remains unclear when precise ages of deposits cannot be accurately determined or interpreted (Deckart et al., 2005; Weihed et al., 2005; Li et al., 2014a). In addition, recognition of areas experienced multiple magmatic-hydrothermal episodes might be a critical factor for recognizing higher grade porphyry or skarn deposits (Vry et al., 2010; Li et al., 2014a; Hu et al., 2015; Spencer et al., 2015; Zhang et al., 2015b). Precise dating of magmatic-hydrothermal events thus may be particularly important for understanding the origin of high-grade ores in certain districts. Applying a combination of reliable geochronological tools, including U–Pb, Re–Os, and $^{40}Ar/^{39}Ar$ isotopic systems to date hydrothermal events, commonly reflected by crosscutting relationships observed in the field, was recommended by Chiaradia et al. (2013) to bracket the timing of a magmatic-hydrothermal episodes.

Iron skarn deposits are one of the more economically important sources of Fe in China, hosting high-grade ores (TFe > 50%) and

* Corresponding author at: MLR Key Laboratory of Metallogeny and Mineral Assessment, Institute of Mineral Resources, Chinese Academy of Geological Sciences, No. 26 Baiwanzhuang Road, Beijing 100037, People's Republic of China.
E-mail address: xieguiqing@cags.ac.cn (G. Xie).

http://dx.doi.org/10.1016/j.oregeorev.2017.01.027
0169-1368/

showing a concentric distribution in some districts (Zhang et al., 2014). The Edong district is a well-endowed Fe skarn cluster located in the western part of the Middle–Lower Yangtze River metallogenic belt (MLYRB), Eastern China (Fig. 1) (Pan and Dong, 1999; Mao et al., 2011; Pirajno and Zhou, 2015). This district is characterized by high-grade Fe and Fe-Cu skarn deposits genetically associated with Late Mesozoic intermediate to felsic intrusions (Shu et al., 1992; Xie et al., 2011b, 2012; Mao et al., 2011). Based on 25 new ages (Re–Os, $^{40}Ar/^{39}Ar$, and U–Pb) and existing data, Li et al. (2014a) demonstrated that the prolonged and episodic magmatic and hydrothermal activity had played significant roles in the formation of high-grade Fe skarn deposits in the Edong district. This has also been partly proven by other recent research on geochronology of the skarn deposits and magnetite textures in the Edong district (Hu et al., 2015; Li et al., 2016; Yao et al., 2015). However, whether multiple magmatic and (or) hydrothermal episodes had occurred in a specific deposit or ore field remains unclear.

The Jinshandian ore field is situated in the western part of the Edong district, and consists of several high-grade Fe skarn deposits, including Zhangfushan, Yuhuasi, Kejiashan, Zhangjingjian, and Liwanlong, which surround the Jinshandian pluton (Fig. 2). The pluton is the product of multiple episodes of magmatism ranging from granitic to dioritic in composition (Shu et al., 1992). Previous K–Ar and Rb–Sr dating loosely bracketed the emplacement age of the Jinshandian pluton (142–90 Ma, K–Ar on whole rock) and Fe mineralization (128–117 Ma, K–Ar and Rb–Sr on phlogopite) in the Jinshandian ore field (cf. Shu et al., 1992). Recent studies revealed that the granite and quartz diorite of the Jinshandian intrusion formed between 133 and 127 Ma based upon LA-ICP-MS zircon U–Pb geochronology, with a mineralization age of about 131 Ma was determined for the Zhangfushan skarn deposit on hydrothermal phlogopite by the $^{40}Ar/^{39}Ar$ dating method (Xie et al., 2012). Ages of other phases from the Jinshandian pluton and other deposits in the Jinshandian ore field are not well constrained. Thus, additional study is critical in the Jinshandian ore field to determine whether high-grade Fe skarn deposits were formed by multiple magmatic-hydrothermal events. This would help corroborate whether ore formation within a single deposit, as well as within the entire Edong district, was continuous or episodic (Wang and Song, 1996; Deckart et al., 2005; Xie et al., 2011b, 2012; Chiaradia et al., 2013; Li et al., 2014a; Yao et al., 2015). Moreover, a more thorough precise age dataset for the entire ore field would be fundamental for a regional comparison between the Fe skarn and magnetite-apatite deposits from the MLYRB. The former deposits occur mainly in the Edong district, whereas the latter are mainly located in the Lingwu and Luzong districts (Fig. 1) in the MLYRB (Mao et al., 2011).

In this contribution, we present new U–Pb geochronological data for magmatic zircon and hydrothermal titanite, and $^{40}Ar/^{39}Ar$ ages for hydrothermal phlogopite from four Fe skarn deposits in the Jinshandian ore field, Edong district. We integrate previous geochronological data with those from this study to better establish the timing of the magmatic-hydrothermal activity, and to determine whether or not multiple magmatic-hydrothermal events took place in the Jinshandian area. Furthermore, this will allow a detailed comparison between timing of Fe skarn formation in the Edong district in the western part and magnetite-apatite deposit formation in the eastern part of the MLYRB.

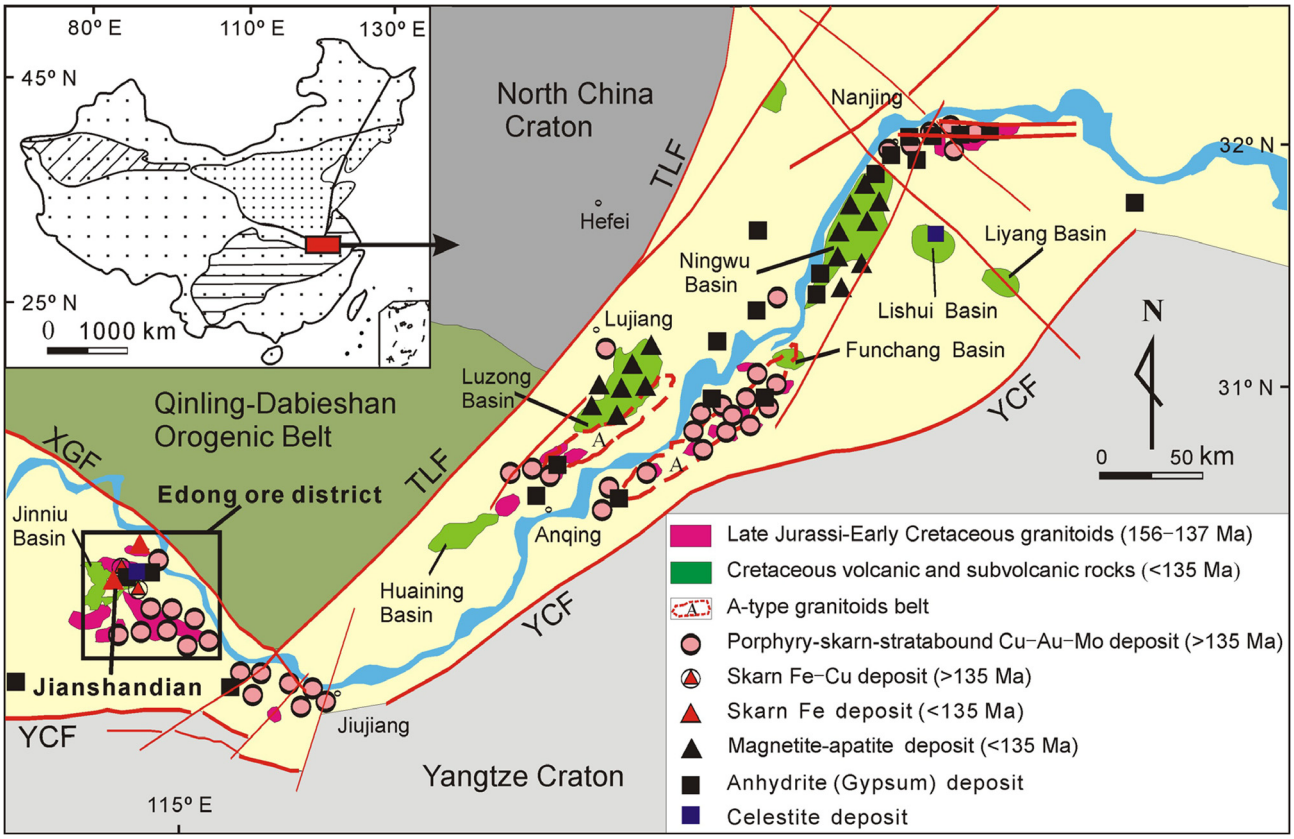

Fig. 1. Sketch map showing the distribution of Fe–Cu, anhydrite (gypsum), and celesite deposits along the Middle–Lower Yangtze River metallogenic belt (modified from Fan et al. (1995), Mao et al. (2011)). (*Abbreviations:* XGF–Xiangfan-Guangji Fault; TLF–Tancheng-Lujiang Falut; YCF–Yangxin-Changzhou Fault.)

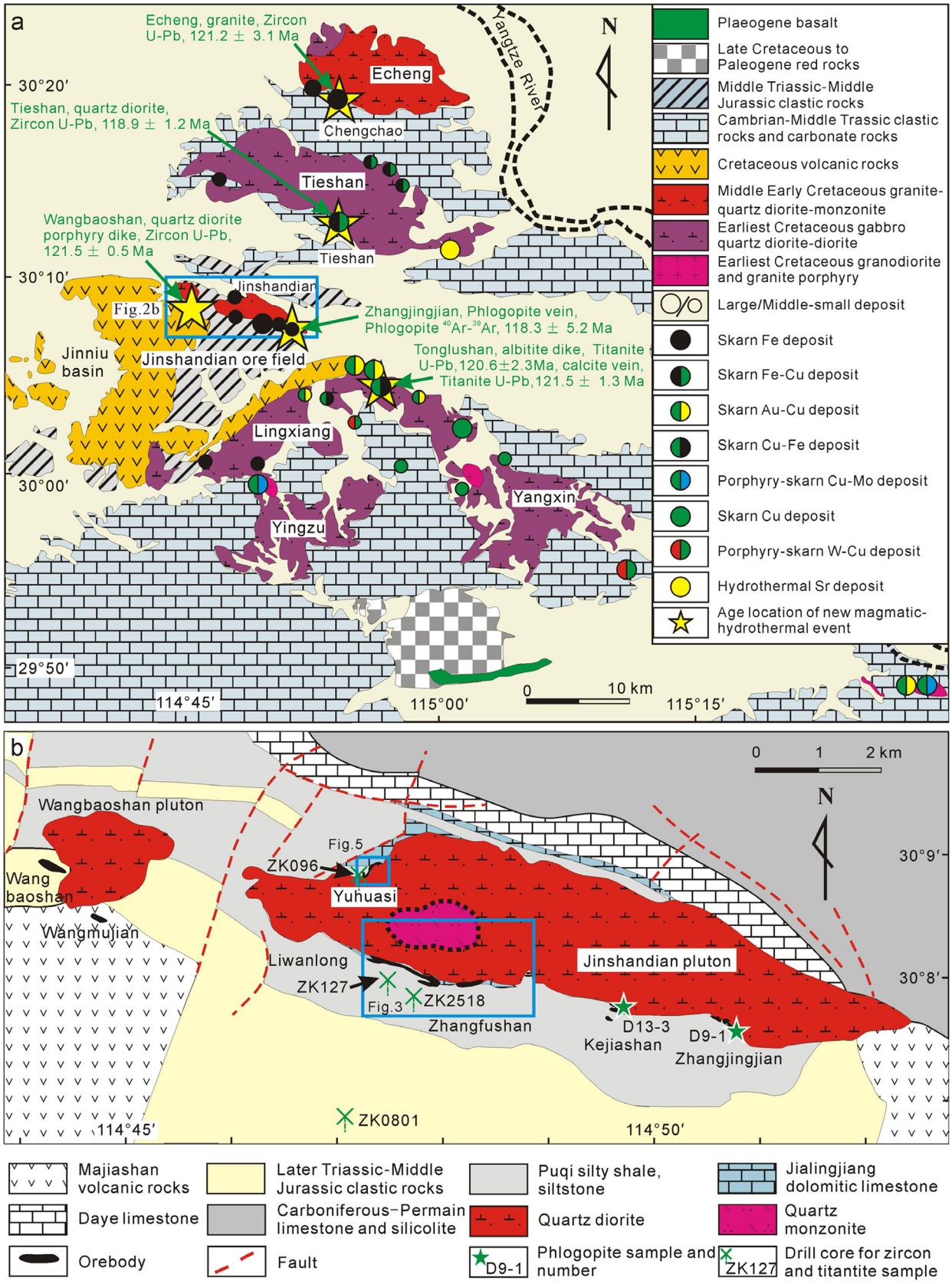

Fig. 2. Geological sketch map of the Edong district (a) and Jinshandian Fe skarn ore field (b) (Fig. 2a was modified from Xie et al. (2015); Fig. 2b was modified from the original maps provided by Central South Geo-Exploration Institute). Ages of new episode of magmatic-hydrothermal activity are shown as green words in Fig. 2a, see text for explanations and data sources. (For interpretation of the references to color in this figure legend, the reader is referred to the web version of this article.)

2. Geological setting and ore geology

2.1. Geological setting

The MLYRB extends along the northern margin of the Yangtze Craton, the southeastern margin of the North China Craton, and the Dabieshan orogenic belt (Fig. 1, Zhai et al., 1996; Mao et al., 2011). The belt is characterized by three stratigraphic sequences, including Archean-Proterozoic metamorphic rocks, Cambrian to Middle Triassic marine sedimentary rocks, and Late Triassic to Cretaceous terrigenous clastic and volcanic rocks (Chang et al., 1991). The basement rocks comprise Archean to Middle Proterozoic metabasalt, phyllite, and slate, intercalated with 2900–990 Ma metaspilite and keratophyre. Rocks of the metamorphic basement are unconformably overlain by shallow marine carbonates and clastic sediments that were deposited in a stable trough (e.g., Chang et al., 1991). The Lower–Middle Triassic sedimentary rocks consist of dolomite, limestone, marl, siltstone, and hundreds of meters of gypsum interbeds, which make the MLYRB an area with important evaporite-bearing sedimentary sequences (Zhai et al., 1996). A series of rift basins formed in the Jurassic-Cretaceous indicate a period of extensional tectonics, which was associated with the formation of the MLYRB, and with deposition of lake- and swamp-facies sandstone, siltstone, and shale, followed by extensive shoshonitic volcanism (Chang et al., 1991; Pan and Dong, 1999). These volcanic and volcano-clastic rocks have been deposited in the period from 135 to 125 Ma by SHRIMP and LA-ICP-MS zircon U–Pb dating methods (Zhang et al., 2003; Hou and Yuan, 2010; Yuan et al., 2010a; Xie et al., 2011a; Zhou et al., 2011a). Rocks of different ages host different types of mineral deposits and are important in different geographic regions (Zhai et al., 1996). For example, Cu- and Au-rich deposits are mainly hosted by upper Paleozoic to Lower Triassic strata, whereas the wall rocks for Fe-rich deposits are mainly of Lower Triassic to Cretaceous age.

This MLYRB comprises seven ore districts, including Edong (southeastern Hubei province), Jiurui (Jiujiang–Ruichang), Anqing-Guichi, Luzong, Tongling, Ningwu, and Ningzhen from west to east. The ore-related igneous rocks in the MLYRB can be divided into three types: (1) 156–137 Ma K-rich calc-alkaline diorite, granodiorite, granite, and granodiorite porphyry bodies, which are associated with 148–135 Ma porphyry-skarn-stratabound Cu–Au––Mo deposits; (2) 135–123 Ma calc-alkaline intrusions consisting of gabbro, pyroxene diorite, quartz diorite, quartz monzonite, granodiorite, granite, diorite porphyry, and granodiorite porphyry intrusions, and their corresponding extrusive equivalents, genetically associated with 135–123 Ma magnetite-apatite and Fe-only skarn deposits; and (3) 127–123 Ma A-type granitoids, associated with Au–U mineralization and consisting of quartz syenite, syenite, quartz monzonite, alkaline granite, and their corresponding volcanic rocks (Fan et al., 2008; Zhou et al., 2008a, 2016; Chen et al., 2011; Mao et al., 2011; Wang et al., 2016). The first type developed mainly in areas of regional uplift, including the Jiurui, Anqing-Guichi, Tongling, and Ningzhen districts. The second type is recognized in Cretaceous volcanic basins and the transitional area between the uplifted areas and volcanic basins, which hosts the Luzong and Ningwu districts and Edong district, respectively (Zhai et al., 1996; Pan and Dong, 1999; Mao et al., 2011). The third type occurs in both the uplifted areas and volcanic basins, along a narrow zone within the eastern part of the MLYRB (Fig. 1, Fan et al., 2008; Zhou et al., 2010).

The Edong Fe–Cu district is located in the westernmost part of the MLYRB (Fig. 1). In this region, Late Proterozoic basement rocks are poorly exposed in the south. The Cambrian to Middle Triassic marine carbonate rocks, clastic rocks, and flysch successions, >6000 m in total thickness, are widespread. They include a gypsum-bearing carbonate layer (>100 m) hosted in Lower to Middle Triassic and minor Upper Triassic to Middle Jurassic clastic rocks (Shu et al., 1992). Cretaceous volcano-sedimentary rocks were deposited in the Jinniu basin (Fig. 2a) in the western part of the Edong district. The volcanic rocks have been dated between 130 and 125 Ma by SHRIMP and LA-ICP-MS zircon U–Pb methods (Xie et al., 2011a).

The Lower to Middle Triassic sedimentary rocks are the most important hosts for the mineralization in the Edong district (Shu et al., 1992). Rocks of the Lower to Middle Triassic Daye Formation and the Lower to Middle Triassic Jialingjiang Formation contain about 50% of the iron reserves, as well as more than 90% of the copper reserves (Fig. 2a), whereas those of the Middle Triassic Puqi Formation contain at least 40% of the iron reserves (Zhai et al., 1996). The main types of mineral occurrences are Fe-only skarn (Zhangfushan, Chengchao), Fe-Cu skarn (Tieshan), Cu-Fe skarn (Tonglushan), and Cu-Mo skarn-porphyry (Tongshankou) deposits (Fig. 2a). The Fe skarn deposits are generally associated with the granite, quartz diorite, and quartz monzonite in the western part of the Edong district, and occur at the contact between granitoid intrusions and Lower to Middle Triassic evaporite-bearing carbonate and clastic rocks (Chang et al., 1991). The Fe-Cu and Cu-Fe skarn deposits are located in the central part of the Edong district, and are genetically related to diorite, quartz diorite, and granodiorite. The Cu–W–Mo skarn-porphyry deposits are associated with granodiorite porphyry stocks in the southeastern part of the district (Fig. 2a).

2.2. Deposit geology

The Jinshandian Fe ore field is located in the western part of the Edong district and contains about 200 million tons (Mt) ore. The ore field includes one large deposit, Zhangfushan, and several medium to small deposits including Yuhuasi, Kejiashan, Zhangjingjian, and Liwanlong. All the deposits are developed surrounding the Jinshandian pluton (Fig. 2b). These deposits share similar geological characteristics with the Tieshan Fe skarn deposit (Zhao et al., 1990; Pan and Dong, 1999), and the below description is based upon observations at the two main deposits, Zhangfushan and Yuhuasi, which are presently in operation.

The Jinshandian pluton has a fusiform shape and strikes NWW along its long axis (Fig. 2b). It consists of quartz diorite, quartz monzonite, pyroxene diorite, diorite, and minor quartz diorite porphyry dikes. The mineralization related igneous rocks are dominantly quartz diorite and quartz monzonite (Shu et al., 1992). Zircon U–Pb isotope studies indicate that the Jinshandian pluton was emplaced between 133 and 127 Ma (Xie et al., 2011b) and the Wangbaoshan intrusion, which is the western outcropping part of the Jinshandian pluton, was emplaced at 132 Ma (Li et al., 2009). The Jinshandian pluton has a wide range in SiO_2 content (48.45–73.89%), relatively low Sr/Y (4–31 ppm) and $(La/Yb)_N$ ratios (3.84–19.50), high Yb content (1.86–3.51 ppm), and variable Eu anomalies ($\delta Eu = 0.35–1.16$). These geochemical features are distinct from the granitic intrusions associated with the Tieshan and Tonglushan Cu–Fe deposits (Fig. 2) (Xie et al., 2008).

The Lower–Middle Triassic strata constitute the country rocks immediately adjacent to or in the vicinity of the orebodies (Fig. 2b). The Lower Triassic Daye Formation is composed of gray thick-bedded limestone and dolomitic limestone that is intercalated with calcareous shale-bearing limestone. The Lower to Middle Triassic Jialingjiang Formation is composed of thin to thick beds of dolomitic limestone, limestone, argillaceous limestone, and calcareous shale, intercalated with thick evaporites. The Middle Triassic Puqi Formation is composed mainly of purplish red silty shale, siltstone, and sandstone. Of the above units, rocks of

the Jialingjiang and Puqi Formations are the most important hosts for the Fe skarn deposits in the Jinshandian ore field (Shu et al., 1992).

2.3. Zhangfushan deposit

The Zhangfushan is the largest deposit in the Jinshandian ore field, with a total resource of 168.6 Mt ore @ 42.3%, including more than 50 Mt of high-grade ores (TFe > 50%) (Shu et al., 1992; Yao et al., 1993). Cobalt and anhydrite are by-products of the iron mining. More than 100 iron orebodies have been identified at Zhangfushan and most of them are located in the center of the southern contact between the Jinshandian pluton and the carbonate and clastic units, with local areas of mineralization extending into the pluton and (or) clastic units (Fig. 3b). Individual orebodies are mainly lenticular or vein-like in shape, are 100–2600 m long and 10–130 m wide, and have a combined length of approximately 3.5 km (Fig. 3a). The orebodies extend for more than 1000 m along trend to the south to southwest, with moderate to high dip angles (57–78°), and are controlled by a NW- to NWW-striking fault along the contact between the pluton and wall rocks (Fig. 3b). The No. I and II orebodies account for 96% of the total Fe reserve of the deposit (Yao et al., 1993). Ore minerals include mainly magnetite, lesser hematite, pyrite, and anhydrite/gypsum, and minor siderite, chalcopyrite, and sphalerite. Gangue minerals are mainly diopside, phlogopite, scapolite, amphibole, and chlorite, with minor calcite, serpentine, garnet, titanite, and epidote. According to the mineral assemblages and textures, four types of ore can be classified as follows: (1) diopside + magnetite ore, (2) phlogopite + diopside + magnetite ore, (3) phlogopite + magnetite ore, and (4) less important anhydrite + magnetite ore.

The intrusion and country rocks at the Zhangfushan deposit have been subjected to extensive hydrothermal alteration, resulting in the formation of a wide variety of skarn and other alteration assemblages (Fig. 4). The host rocks surrounding the deposits also have been pervasively changed to marble and hornfels (Fig. 3a, b). An obvious skarn zonation has developed from within the margin of the quartz diorite intrusion outward to the wall rocks in the Zhangfushan open pit (Fig. 4). As shown in the profile, quartz diorite is exposed at the top and east of the mountain, with the density of diopside veins in the quartz diorite being greatest there (Fig. 4a, d). These then change to diopside + amphibole stockworks (Fig. 4c) downward and towards west, and subsequently change outward to massive amphibole + epidote endoskarn with remnant quartz diorite (Fig. 4b). Massive phlogopite exoskarn that hosts magnetite ore is located at the foot of the mountain and to the left side of the profile (Fig. 4a, b). On the basis of crosscutting relationships and mineral assemblage studies, prograde and retrograde events can be distinguished, with each including two sub-stages. The general sequence of mineralization at Zhangfushan is (diopside/scapolite-garnet) → (magnetite-phlogopite/amphibole-epidote-albite) → (anhydrite-pyrite-chlorite) → (calcite-gypsum/pyrite). Three main skarn types associated with Fe mineralization are recognized, including diopside skarn, scapolite skarn, and phlogopite skarn.

2.4. Yuhuasi deposit

The Yuhuasi deposit is located along the northwestern margin of the Jinshandian pluton, at its contact with carbonate and clastic rocks (Figs. 2 and 6). It has a resource of 14.7 Mt ore @ 35.2% Fe, as well as about 2 Mt of anhydrite/gypsum reserves as by-products. Six iron orebodies and several anhydrite/gypsum orebodies have been discovered. The individual orebodies are crescent or lenticular in shape, and are 30–760 m long and 5–80 m wide, with a cumulative length of approximately 800 m and a width of 450 m (Fig. 6a). The orebodies extend for more than 450 m along trend to the south to southwest, with moderate to high dip angles (45–70°) (Fig. 6b). The No. I iron orebody accounts for 97% of the total Fe reserve. Anhydrite/gypsum orebodies were discovered at 200 m below sea level in the southern part of the deposit. They were developed within the dolomitic marble or at the contact between the iron orebody and hornfels (Fig. 6b). Ore minerals include magnetite, lesser hematite, pyrite, and anhydrite/gypsum, and minor chalcopyrite. Gangue minerals are phlogopite, chlorite, diopside, calcite, and scapolite, with minor amphibole, serpentine, garnet, and epidote. Based upon the mineral assemblages, textures, and the conditions of formation, three types of Fe ore can be classified as follows: (1) diopside + magnetite ore, (2) phlogopite + diopside + magnetite ore, and (3) phlogopite + magnetite ore. Types 1 and 3 are the most important Fe ores. Large amounts of hornfels breccia were recognized in an anhydrite/gypsum orebody

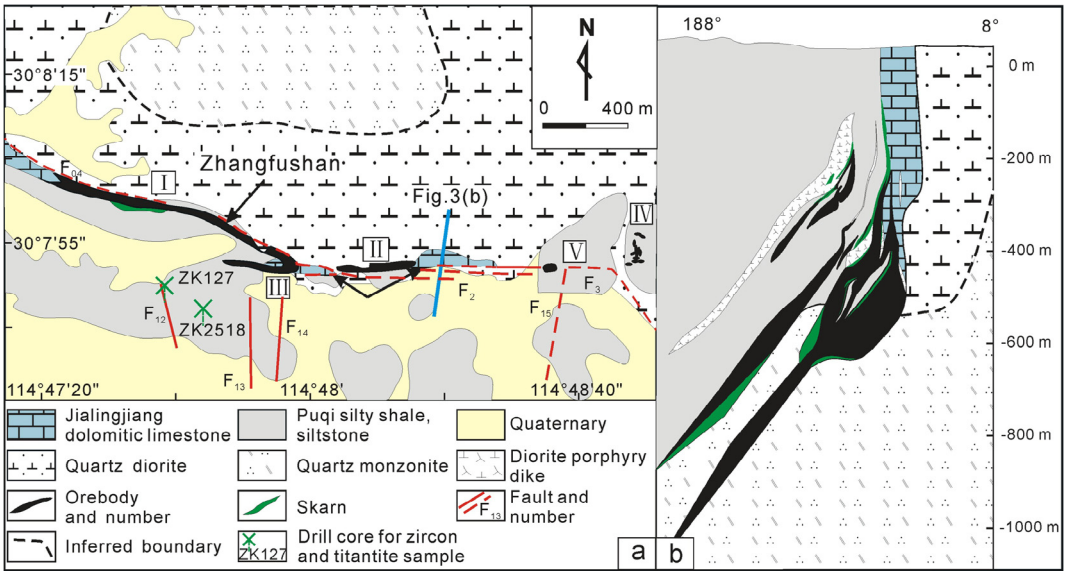

Fig. 3. Geological sketch map (a) and No. 39 geological section map (b) of the Zhangfushan deposit (modified from Yao et al. (1993) and Zhu et al. (2015)).

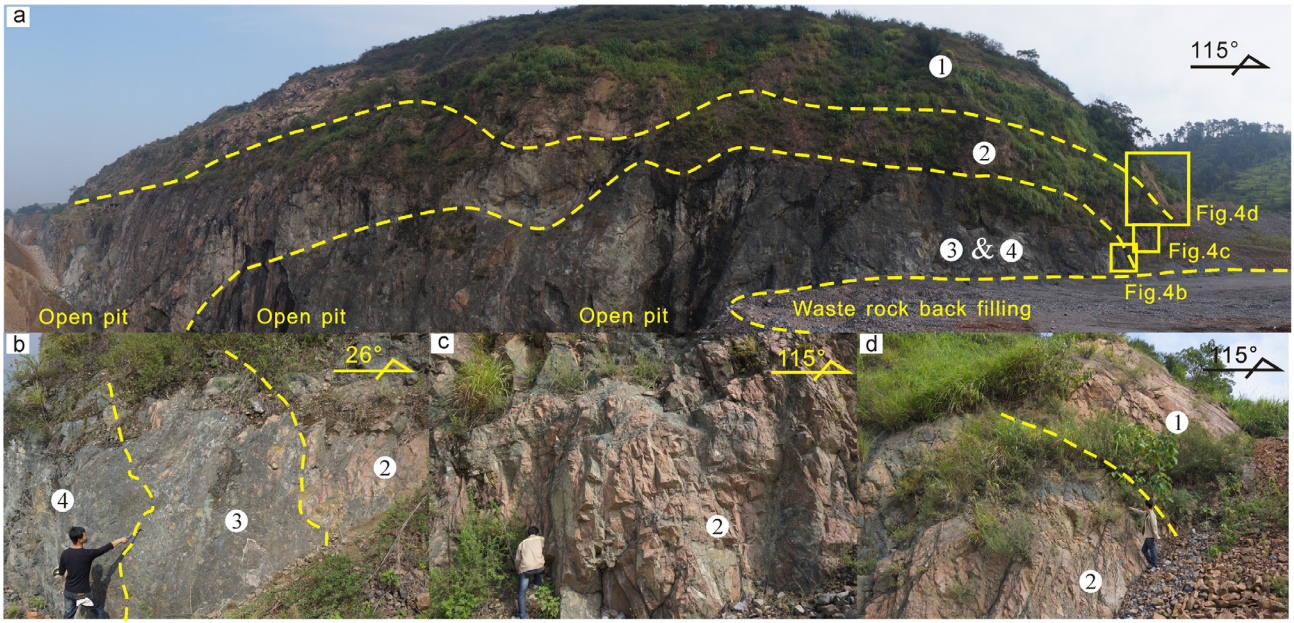

Fig. 4. Overall view and skarn zonation of the open pit at the Zhangfushan deposit. ① fresh quartz diorite; ② quartz diorite with diopside + amphibolite stockworks; ③ massive amphibolite skarn with remnant quartz diorite ④ massive phlogopite skarn.

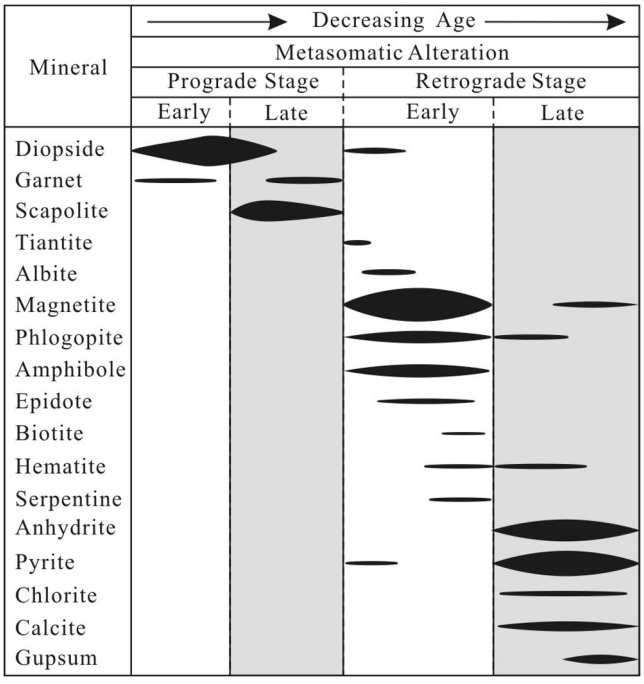

Fig. 5. Paragenetic sequence of mineralization and alteration in the Zhangfushan deposit (after Zhu et al., 2015).

near the hornfels. The hornfels breccia in the anhydrite/gypsum orebodies is zoned form a central fresh sandstone, to chloritized sandstone, then to a thin phlogopite zone, and finally to magnetite ore with minor pyrite at the margin. The entire breccia was cut by a late gypsum vein (Zhu et al., 2015). The alteration and skarn mineral assemblages at the Yuhuasi deposit are similar to those at the Zhangfushan deposit. Diopside and scapolite are the main skarn minerals formed during the prograde stage, with magnetite, phlogopite, pyrite, calcite, anhydrite, and gypsum developed in the retrograde stage.

3. Sampling and analytical methods

3.1. Sampling

Eight samples were chosen for the isotope analysis in this study. A sample of fine-grained quartz monzonite (JS520) was taken from drill core ZK096 at the Yuhuasi deposit (Figs. 2b, 6a and 7a). It consists of plagioclase (40–50%), K-feldspar (35–40%), and quartz (10–15%), with accessory magnetite, titanite, zircon, and apatite. The intergrowth of K-feldspar and quartz reveals a micrographic texture (Fig. 7d). Quartz diorite samples JS218 and JS328 were collected from an underground adit at 256 m below sea level in the Yuhuasi deposit and at 878.0 m below surface in drill core ZK0801 of the Chenjiawan occurrence (about 2.5 km southwest of the Zhangfushan deposit, Fig. 2b) respectively. Both of these samples are fine-grained quartz diorite, which consists of plagioclase (50–65%), K-feldspar (10–20%), quartz (5–15%), and minor amphibole and biotite (Fig. 7b, e), as well as accessory magnetite, titanite, zircon, and apatite. A sample of fine-grained quartz diorite porphyry dike (JS239) was obtained from drill core ZK2518 at the Zhangfushan deposit (Figs. 2b and 3a). The quartz diorite porphyry crosscutting the magnetite orebody was observed in an underground adit (Fig. 7c). It has a porphyritic texture and the phenocryst includes plagioclase (5–15%) and quartz (5–8%), as well as minor augite, amphibolite, and K-feldspar, surrounded by a matrix of similar minerals (Fig. 7f). Accessory minerals are magnetite, titanite, apatite, and zircon. All of the igneous samples experienced weak sericite, carbonate, and chlorite alteration (Fig. 7d, e).

Titanite sample JS444 was taken from the scapolite + diopside skarn in drill core ZK127 at the Zhangfushan deposit (Figs. 2b and 3a). Coarse titanite grains in the sample are present as a vein that crosscuts diopside skarn, where they replace scapolite and diopside (Fig. 8a, b). The titanite grains were subsequently replaced by Fe–Ti oxide (ilmenite + ulvospinel + magnetite)+pyrite (Fig. 8c, d, e, f) and the titanite vein is cut by an anhydrite vein (Fig. 8a). Titanite sample JS558 was collected from a pyrite + anhydrite + chlorite + apatite + titanite + calcite metasomatic rock in drill core ZK127 at the Zhangfushan deposit (Figs. 2b and 3a). Titanite occurs as disseminated medium to coarse grains

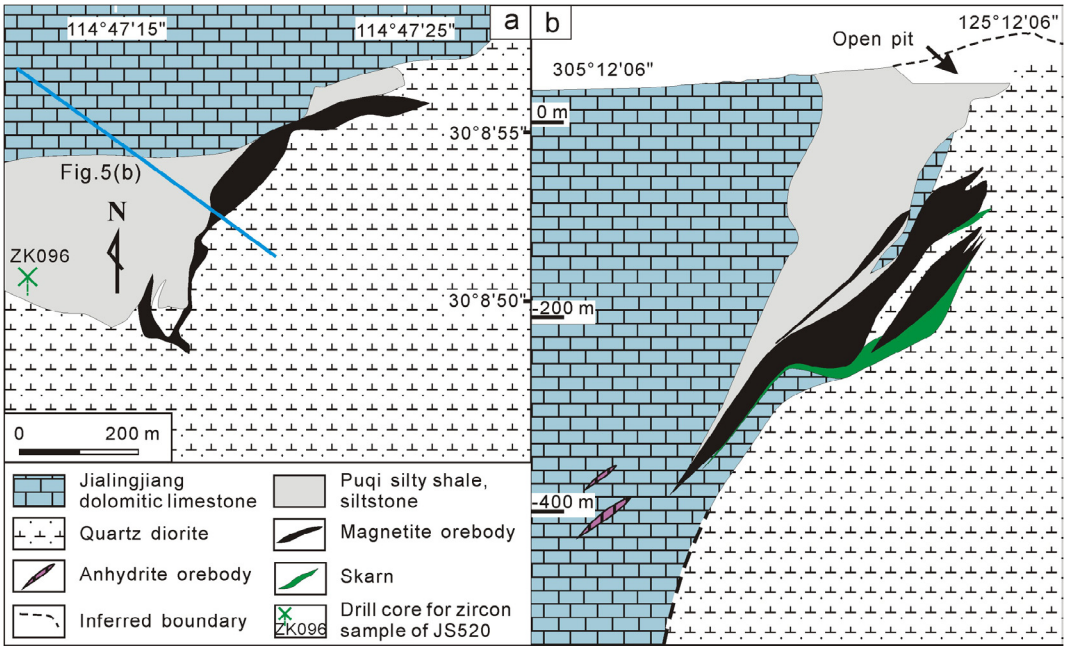

Fig. 6. Geological sketch map (a) and No. 6 geological section map (b) of the Yuhuasi deposit. The original maps were provided by Central South Geo-Exploration Institute and updated from our own field observations.

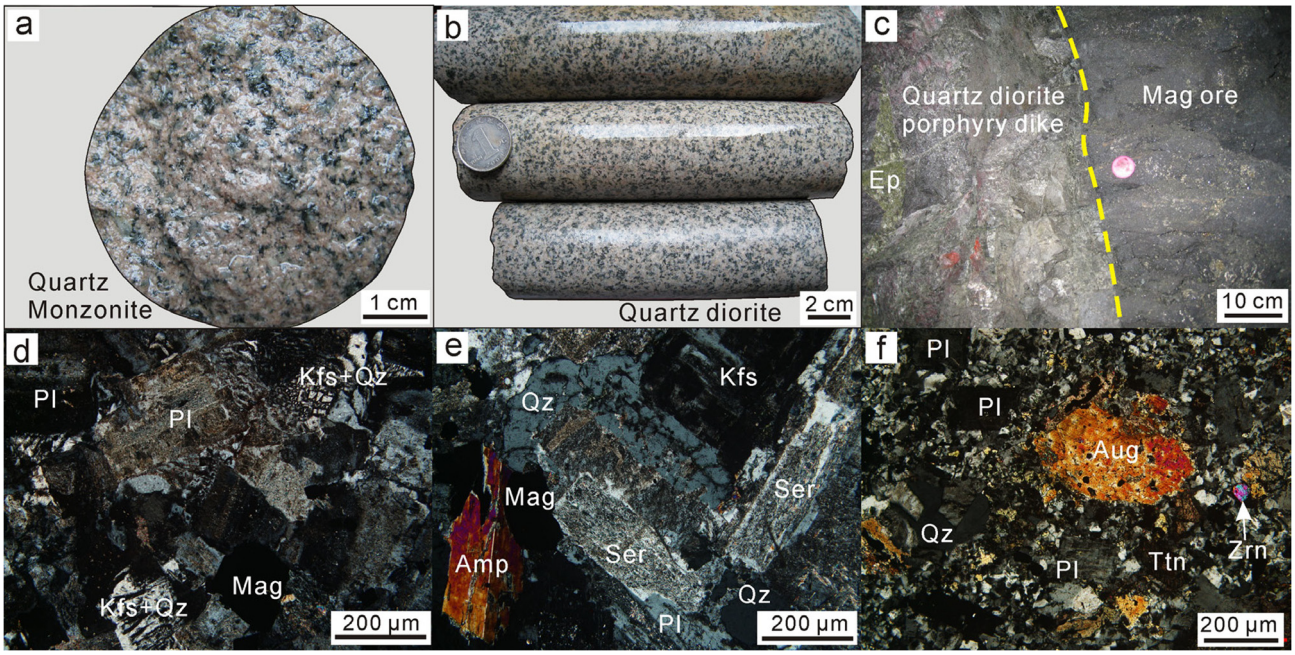

Fig. 7. Characteristic features, field aspects, and photomicrographs of the igneous rocks of the Jinshandian pluton. (a) Diopside + chlorite skarn between the quartz monzonite and massive magnetite orebody, some skarn veinlets developed in the quartz monzonite; quartz monzonite shows a micrographic texture, with K-feldspar intergrown with quartz and surrounding plagioclase, which developed different degrees of carbonization, biotite and magnetite also can be recognized (d). (b) Sample of quartz diorite with weak carbonization (e). (c) Quartz diorite porphyry dike intruding massive magnetite orebody and showing epidotization near the contact between the dike and orebody; plagioclase, quartz, and minor augite as phenocrysts. (d–f) Cross-polarized transmitted light. (*Abbreviations:* Aug–augite, Bi–Biotite, Chl–chlorite, Di–diopside, Ep–epidote, Kf–K-feldspar, Mag–magnetite, Pl–plagioclase, Py–pyrite, Q–quartz, Ser–Sericite.)

(Fig. 8g, h). Phlogopite sample D10-3 was collected from the dismissed magnetite ore in the open pit at the Kejiashan deposit (Fig. 2b). Phlogopite is intergrown with anhedral-subhedral magnetite and parts of the grains are replaced by serpentine (Fig. 8i, j). Coarse-grained phlogopite sample D9-1 was collected from a phlogopite vein that crosscuts the magnetite ore in the open pit at the Zhangjingjian deposit (Figs. 2b and 8l). Minor anhedral magnetite and pyrite fill interstices between phlogopite crystals, and parts of the phlogopite grains were replaced by serpentine and magnetite (Fig. 8m, n).

3.2. Analytical methods

3.2.1. LA-ICP-MS zircon U–Pb dating

Zircon grains were extracted by conventional heavy liquids and magnetic techniques, and then purified by hand-picking under a

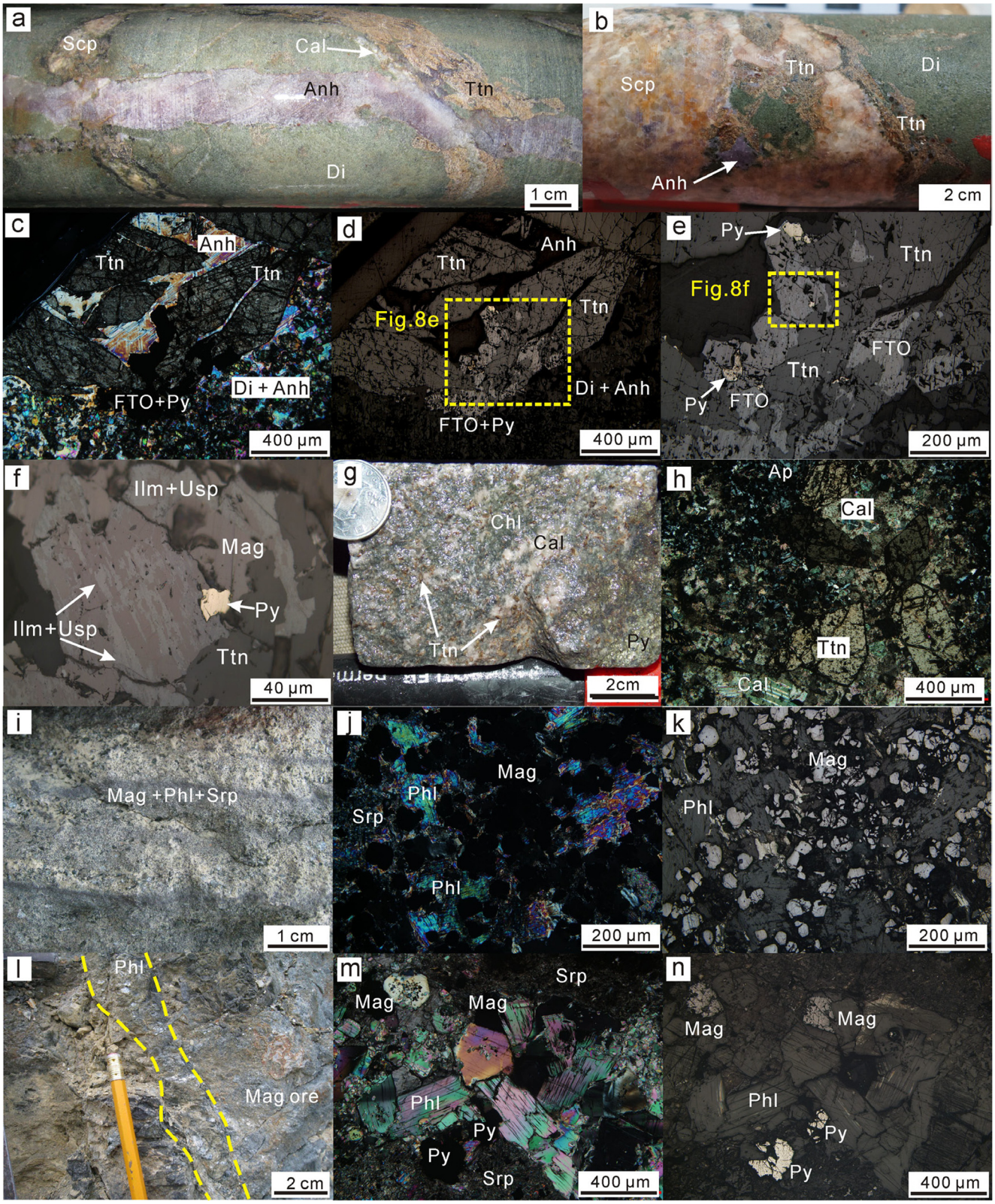

Fig. 8. Characteristic features, field aspects, and photomicrographs of the titanite and phlogopite sample. (a, b) Titanite occurs as veins or inhomogeneous coarse grains and replaces scapolite and diopside, then the titanite vein was cut by an anhydrite vein. (c–f) Margin of the titanite grains was replaced by Fe-Ti oxide(ilmenite + ulvöspinel + magnetite) + pyrite (c–e). (g–h) Medium to coarse grains of titanite well-distributed in pyrite + anhydrite + chlorite + apatite + titanite + calcite metasomatic rock. (i–k) Phlogopite in dismissed magnetite ore in the open pit of the Kejiashan deposit, Phlogopite is found intergrown with anhedral-subhedral magnetite and part of phlogopite grains were replaced by serpentine. (l) Phlogopite vein cuts magnetite ore in the open pit at Zhangjingjian deposit, phlogopite in the vein as coarse grains with minor magnetite and pyrite filling the interstices between crystals (m–n). (c, h, j and m) Cross-polarized transmitted light; (d, e, f, k and n) reflected light. (*Abbreviations:* Anh–anhydrite, Ap–apatite, Cal–calcite, Di–diopside, FTO–Fe-Ti oxide, Ilm–ilmenite, Mag–magnetite, Phl–phlogopite, Py–pyrite, Scp–scapolite, Srp–serpentine, Tnn–titanite, Usp–ulvöspinel.)

binocular microscope. Representative zircon grains were mounted in epoxy resin and polished to expose the grain center. Prior to analysis, all zircon grains were photographed in transmitted, reflected light and cathodoluminescence (CL) to examine the inner structures, fluid inclusions, and cracks for further selecting suitable crystals and test points. The U–Pb isotope analyses were undertaken by using a Finnigan Neptune inductively coupled plasma mass spectrometer that was connected to a NewWave UP-213 laser ablation (LA-MC-ICP-MS) at the Institute of Mineral Resources, Chinese Academy of Geological Sciences, Beijing, China. Details about the instrument protocols and data acquisition methods used during this study are described by Hou et al. (2007). Helium was used as a carrier gas to enhance transport efficiency of the ablated materials, and argon was used as a make-up gas and mixed with helium via a T-connector before entering the MC-ICP-MS. The analytical procedures used were identical to those described by Hou and Yuan (2010). The external standard GJ-1 was analyzed twice every 5–10 analyses to monitor the age of zircon grains. Data were processed according to the procedure of Liu et al. (2010), and the Isoplot program (version 3.0, Ludwig, 2003) was used for U–Pb age calculations and concordia diagram construction. Age uncertainties are cited as 1σ value, and weighted mean $^{206}Pb/^{238}U$ ages are quoted at the 95% confidence limit (2σ).

3.2.2. LA-ICP-MS titanite U–Pb dating

Titanite sample preparation was similar to that for the zircons. Titanite grains were extracted by conventional heavy liquids and magnetic techniques, and then purified by hand-picking under a binocular microscope. Representative titanite grains were mounted in epoxy resin and polished to expose the grain center. Prior to analysis, all titanite grains were photographed in transmitted, reflected light and Back Scattered Electron imaging (BSE) to examine the inner structures, fluid inclusions, and cracks for further selecting suitable crystals and test points. Analyses for titanite U–Pb dating were conducted using laser ablation inductively coupled mass spectrometry (LA-ICP-MS) at the State Key Laboratory of Lithospheric Evolution, Institute of Geology and Geophysics, Chinese Academy of Sciences, Beijing, China. The detailed analytical procedures are similar to those for zircon as described by Sun et al. (2010) and Yang et al. (2009). The Pulse/Analogy (P/A) factor was corrected using the P/A calibration solution before routine analysis. A tuning solution was also used to optimize the instrumental parameters to yield productivities of oxide (CeO^+/Ce^+) and doubly charged Ce^{2+}/Ce^+ of less than 1% and 3%, and sensitivity for ^{89}Y better than 200 Mcps/ppm. During laser-ablation, the instrument was optimized using NIST SRM 610 standard glass. The detailed parameters are shown by Sun et al. (2012). The ICP-MS measurements were carried out using time-resolved analysis and peak hopping at one point per mass. The dwell times were 10 ms for ^{29}Si, ^{43}Ca, ^{232}Th, and ^{238}U, 15 ms for ^{204}Pb, ^{206}Pb, and ^{208}Pb, and 30 ms for ^{207}Pb. Each spot analysis consisted of a 30 s background acquisition and 60 s sample data acquisition and 60 s for cleaning the sample cell and plumbing lines. Every eight samples analyzed were followed by two titanite BLR-1 standards, one titanite OLT-1 standard, and one NIST SRM 610 measurement. The 60 μm spot size and 6 Hz ablation frequency were used for single spot analysis.

Uranium, Th, and Pb concentrations were calibrated using ^{43}Ca as the internal calibration for titanite (determined from the average CaO concentration of the sample analyzed by EMPA), using NIST SRM 610 as the reference material. Both titanite standards BLR-1 and OLR-1 were used as the external standard for U–Pb fractionation correction of single spot. The $^{207}Pb/^{206}Pb$ and $^{206}Pb/^{238}U$ ratios were calculated using the program of GLITTER (version 4.0, Griffin et al., 2008). Standard deviations of calibrated isotope ratios include those from samples, external standards (BLR-1 titanite or OLR-1), and reference values. The relative standard deviations of reference values for the external standards were set at 2%. Because the ^{204}Pb signal intensity was much lower than those for the other Pb isotopes and suffered a large isobaric interference from ^{204}Hg, it was difficult to measure accurately (e.g., Sun et al., 2010). The ^{207}Pb method was applied for common Pb corrections through an estimate of $^{207}Pb/^{206}Pb$ (130 Ma, 0.844 ± 0.04) according to the two-stage model for lead (Stacey and Kramers, 1975). Subsequently, weighted mean $^{206}Pb/^{238}U$ ages were calculated using the Isoplot program (version 3.0, Ludwig, 2003). Errors of individual analyses are based on counting statistics and are given at the 1σ level. Trace element concentrations were calculated using the program of GLITTER (version 4.0, Griffin et al., 2008) and calibrated using ^{40}Ca as an internal standard and NIST SRM 610 as an external reference material. The analytical uncertainties are mostly within 10%.

3.2.3. $^{40}Ar/^{39}Ar$ dating

Fresh phlogopite samples were crushed and purified with a magnetic separator and then cleaned by ultrasonic treatment under ethanol. The purity of the mineral grains (0.08–0.15 mm) was more than 99%. Samples were wrapped in aluminum foil and loaded into a tube of aluminum foil, together with two or three monitor samples. The tubes were sealed into a quartz bottle (40 mm high; 50 mm in diameter). The bottle was irradiated for 51 h 46 min in a nuclear reactor (The Swimming Pool Reactor, Chinese Institute of Atomic Energy, Beijing, China). The reactor delivers a neutron flux of 6.0×10^{12} n cm^{-2} s^{-1}. The integrated neutron flux is about 1.16×10^{18} n cm^{-2}. After irradiation, the samples and monitors were removed from the quartz bottle and then loaded into the vacuum extraction system. They were baked out for 48 h at 120–150 °C. The argon extraction system comprises an electron bombardment heated furnace in which the samples are heated under vacuum. A thermocouple was used to monitor and control the temperature of the furnace. The furnace can automatically attain the set temperature and remains within a range of few degrees. The released gases are admitted to a purification system, with 30 min duration for heating-extraction for each temperature increment and 30 min for purification. The purification system uses a U-tube cooled with a mixture of acetone and dry ice, titanium sublimation pump at 38 A filament current, and a titanium sponge furnace at 800 °C. Finally, the gases were purified by two Sorb-AC pumps at room temperature. Purified argon was trapped in an activated charcoal finger at liquid-nitrogen temperature and then released into the MM-1200B Mass Spectrometer to analyze the argon isotopes in the Isotope Laboratory of the Institute of Geology and Geophysics, China Academy of Sciences, Beijing.

Measured isotopic ratios were corrected for mass discrimination, atmospheric argon component, blanks, and irradiation-induced mass interference. The correction factors for interfering isotopes produced during irradiation were determined by analysis of irradiated K_2SO_4 and CaF_4 pure salts, and their values are $(^{36}Ar/^{37}Ar)_{Ca} = 0.000240$, $(^{40}Ar/^{39}Ar)_K = 0.004782$, and $(^{39}Ar/^{37}Ar)_{Ca} = 0.000806$. The blanks of the m/e = 40, m/e = 39, m/e = 37, and m/e = 36 are less than 6×10^{-15}, 4×10^{-16}, 8×10^{-17}, and 2×10^{-17} mol, respectively. The decay constant used is $\lambda = 5.543 \times 10^{-10}$ a^{-1} (Steiger and Jäger, 1977). All ^{37}Ar analyses were corrected for radiogenic decay (half-life 35.1 days). Uncertainty in each apparent age is given at 1σ value. The monitor used is the Fangshan biotite granite (ZBH-25) internal standard, whose age is 132.7 ± 1.2 Ma and potassium content is 7.579 ± 0.030 wt% (Wang, 1983). The Isoplot program (version 3.0, Ludwig, 2003) was used for the plateau age spectrum and $^{40}Ar/^{36}Ar$ vs. $^{39}Ar/^{36}Ar$ isochron and inverse isochron diagrams.

Table 1
LA-MC-ICP-MS U-Pb isotope data for zircon from the Jinshandian ore field.

Sample	Concentration (ppm)			Th/U	Measured isotopic ratios						Ages (Ma)			
	U	Th	Pb		$^{207}Pb/^{206}Pb$	1σ	$^{207}Pb/^{235}U$	1σ	$^{206}Pb/^{238}U$	1σ	$^{207}Pb/^{235}U$	1σ	$^{206}Pb/^{238}U$	1σ
Quartz monzonite														
JS520-1	184	57	62.3	3.24	0.0511	0.0023	0.1461	0.0069	0.0208	0.0003	138.5	6.1	132.6	2.2
JS520-2	91	30	48.7	3.04	0.0488	0.0135	0.1440	0.0402	0.0212	0.0008	136.6	35.7	135.0	5.3
JS520-3	177	91	71.1	1.95	0.0513	0.0015	0.1434	0.0055	0.0203	0.0006	136.1	4.9	129.5	3.6
JS520-4	222	87	68.0	2.54	0.0486	0.0021	0.1352	0.0063	0.0202	0.0003	128.8	5.7	128.8	1.8
JS520-5	34	19	21.1	1.77	0.0512	0.0171	0.1451	0.0477	0.0207	0.0010	137.5	42.3	132.0	6.2
JS520-6	53	22	21.2	2.38	0.0474	0.0085	0.1304	0.0211	0.0202	0.0004	124.4	18.9	128.7	2.7
JS520-7	93	37	22.2	2.47	0.0468	0.0032	0.1318	0.0091	0.0205	0.0002	125.7	8.1	130.6	1.4
JS520-8	65	30	13.7	2.20	0.0499	0.0054	0.1400	0.0155	0.0203	0.0004	133.0	13.8	129.7	2.4
JS520-9	43	21	0.2	2.00	0.0512	0.0086	0.1400	0.0241	0.0199	0.0006	133.0	21.5	127.1	4.0
JS520-10	40	24	0.2	1.67	0.0497	0.0062	0.1388	0.0179	0.0204	0.0004	132.0	16.0	130.0	2.7
JS520-11	47	16	6.9	2.92	0.0485	0.0129	0.1431	0.0427	0.0211	0.0015	135.8	37.9	134.7	9.7
JS520-12	42	19	9.9	2.21	0.0488	0.0062	0.1390	0.0178	0.0205	0.0006	132.1	15.9	130.7	3.9
JS520-13	145	55	40.3	2.62	0.0521	0.0038	0.1480	0.0078	0.0210	0.0012	140.2	6.9	134.0	7.6
JS520-14	87	31	30.9	2.84	0.0471	0.0058	0.1403	0.0286	0.0212	0.0016	133.3	25.5	135.1	10.2
Quartz diorite														
JS218-1	73	30	42.8	2.38	0.0486	0.0021	0.1328	0.0059	0.0198	0.0003	126.6	5.3	126.6	1.7
JS218-2	54	20	26.3	2.63	0.0510	0.0031	0.1366	0.0083	0.0194	0.0004	130.0	7.4	124.2	2.3
JS218-3	43	18	51.0	2.44	0.0487	0.0075	0.1324	0.0206	0.0199	0.0005	126.2	18.4	126.7	3.4
JS218-4	71	30	24.0	2.37	0.0481	0.0024	0.1280	0.0061	0.0196	0.0003	122.3	5.5	125.1	2.0
JS218-5	166	66	92.2	2.54	0.0489	0.0014	0.1369	0.0045	0.0203	0.0004	130.3	4.0	129.9	2.6
JS218-6	33	18	18.2	1.85	0.0501	0.0034	0.1447	0.0113	0.0206	0.0004	137.2	10.0	131.2	2.7
JS218-7	87	26	64.2	3.34	0.0477	0.0034	0.1324	0.0099	0.0200	0.0005	126.3	8.8	127.9	3.1
JS218-8	65	27	53.5	2.39	0.0489	0.0057	0.1382	0.0213	0.0198	0.0005	131.5	19.0	126.4	3.4
JS218-9	95	33	64.4	2.85	0.0512	0.0024	0.1418	0.0069	0.0203	0.0003	134.7	6.2	129.5	2.1
JS218-10	90	35	73.7	2.58	0.0486	0.0031	0.1336	0.0082	0.0200	0.0004	127.3	7.4	127.7	2.7
JS218-11	64	25	60.0	2.54	0.0494	0.0041	0.1331	0.0102	0.0198	0.0004	126.9	9.2	126.6	2.8
JS218-12	58	20	34.7	2.89	0.0509	0.0070	0.1423	0.0194	0.0205	0.0005	135.1	17.2	130.6	3.3
JS218-13	69	23	67.2	2.95	0.0509	0.0056	0.1405	0.0154	0.0200	0.0006	133.5	13.7	128.0	3.6
JS218-14	54	19	32.2	2.81	0.0491	0.0035	0.1322	0.0096	0.0198	0.0004	126.1	8.6	126.2	2.4
JS218-15	50	18	22.9	2.84	0.0490	0.0055	0.1297	0.0119	0.0198	0.0007	123.9	10.7	126.6	4.2
JS218-16	325	69	109.5	4.74	0.0515	0.0101	0.1442	0.0222	0.0205	0.0009	136.7	19.7	130.7	5.7
JS218-17	77	29	11.6	2.67	0.0467	0.0033	0.1264	0.0087	0.0198	0.0004	120.9	7.8	126.2	2.8
JS218-18	48	22	6.1	2.14	0.0488	0.0059	0.1300	0.0147	0.0198	0.0007	124.1	13.2	126.2	4.5
JS218-19	135	33	32.8	4.06	0.0482	0.0032	0.1336	0.0088	0.0202	0.0004	127.3	7.9	128.6	2.8
JS218-20	235	54	62.9	4.37	0.0498	0.0025	0.1395	0.0086	0.0203	0.0006	132.6	7.6	129.4	4.0
JS218-21	102	37	28.0	2.74	0.0470	0.0034	0.1288	0.0093	0.0200	0.0004	123.0	8.4	127.5	2.4
Quartz diorite														
JS328-1	25	20	28.0	1.25	0.0509	0.0056	0.1402	0.0152	0.0202	0.0005	133.2	13.6	129.1	2.9
JS328-2	92	39	38.2	2.34	0.0507	0.0017	0.1393	0.0050	0.0199	0.0002	132.4	4.5	127.3	1.6
JS328-3	163	52	72.8	3.13	0.0511	0.0024	0.1441	0.0077	0.0205	0.0007	136.6	6.9	130.8	4.2
JS328-4	154	59	65.0	2.59	0.0510	0.0047	0.1452	0.0147	0.0206	0.0008	137.6	13.1	131.3	4.8
JS328-5	144	99	55.6	1.45	0.0477	0.0011	0.1322	0.0031	0.0202	0.0003	126.1	2.8	128.7	1.7
JS328-6	83	29	41.9	2.83	0.0481	0.0025	0.1345	0.0070	0.0204	0.0004	128.2	6.3	130.3	2.3
JS328-7	106	37	41.9	2.90	0.0496	0.0022	0.1371	0.0054	0.0203	0.0003	130.5	4.8	129.7	1.9
JS328-8	313	80	129.7	3.92	0.0467	0.0014	0.1291	0.0047	0.0200	0.0003	123.3	4.2	127.6	1.9
JS328-9	114	38	49.0	2.97	0.0481	0.0015	0.1302	0.0041	0.0198	0.0002	124.2	3.7	126.2	1.0
JS328-10	154	39	53.7	3.93	0.0507	0.0024	0.1379	0.0064	0.0199	0.0002	131.2	5.7	127.0	1.1
JS328-11	82	36	32.7	2.26	0.0500	0.0019	0.1384	0.0051	0.0203	0.0002	131.6	4.5	129.2	1.1
JS328-12	103	37	33.4	2.76	0.0486	0.0033	0.1308	0.0085	0.0196	0.0004	124.8	7.6	125.2	2.8
JS328-13	60	24	16.1	2.52	0.0506	0.0095	0.1417	0.0280	0.0202	0.0008	134.5	24.9	129.1	5.3
JS328-14	325	101	96.9	3.20	0.0500	0.0010	0.1368	0.0030	0.0198	0.0002	130.2	2.7	126.7	1.0
JS328-15	310	150	101.3	2.07	0.0482	0.0006	0.1333	0.0019	0.0201	0.0002	127.1	1.7	128.2	1.2
JS328-16	56	21	15.4	2.71	0.0511	0.0037	0.1373	0.0100	0.0198	0.0003	130.6	9.0	126.3	2.1
JS328-17	96	33	36.7	2.93	0.0478	0.0082	0.1362	0.0262	0.0202	0.0006	129.7	23.4	129.1	3.9
JS328-18	165	53	52.2	3.13	0.0513	0.0026	0.1382	0.0070	0.0197	0.0004	131.4	6.3	125.7	2.2
JS328-19	251	91	82.3	2.77	0.0506	0.0010	0.1402	0.0030	0.0202	0.0003	133.3	2.7	128.9	1.7
JS328-20	148	43	36.9	3.43	0.0491	0.0017	0.1332	0.0048	0.0198	0.0002	127.0	4.3	126.4	1.5
JS328-21	339	99	105.2	3.43	0.0491	0.0022	0.1364	0.0062	0.0202	0.0005	129.9	5.5	129.1	2.8
JS328-22	106	35	52.3	2.98	0.0488	0.0030	0.1394	0.0090	0.0208	0.0005	132.5	8.0	133.0	2.9
JS328-23	71	32	37.7	2.25	0.0461	0.0045	0.1257	0.0133	0.0197	0.0007	120.2	12.0	125.4	4.1
JS328-24	1081	466	430.0	2.32	0.0508	0.0005	0.1395	0.0024	0.0199	0.0003	132.6	2.1	127.1	1.8
JS328-25	182	75	103.6	2.42	0.0519	0.0042	0.1445	0.0107	0.0205	0.0008	137.0	9.5	130.5	5.0
JS328-26	61	28	16.7	2.21	0.0504	0.0030	0.1372	0.0079	0.0200	0.0003	130.5	7.0	127.8	2.0
JS328-27	221	93	91.0	2.36	0.0509	0.0012	0.1392	0.0034	0.0199	0.0002	132.3	3.0	127.0	1.5
Quartz diorite porphyry dike														
JS239-1	104	49	29.1	2.14	0.0488	0.0018	0.1334	0.0053	0.0198	0.0003	127.1	4.8	126.5	1.9
JS239-2	177	65	50.2	2.70	0.0472	0.0024	0.1295	0.0078	0.0199	0.0006	123.6	7.0	126.8	3.6
JS239-3	81	32	24.8	2.57	0.0504	0.0072	0.1335	0.0208	0.0195	0.0009	127.3	18.6	124.8	5.8
JS239-4	72	40	25.3	1.78	0.0505	0.0018	0.1367	0.0055	0.0196	0.0003	130.1	4.9	125.0	1.8
JS239-5	66	32	39.2	2.05	0.0507	0.0041	0.1339	0.0116	0.0192	0.0004	127.6	10.4	122.4	2.6
JS239-6	76	29	23.3	2.62	0.0504	0.0028	0.1356	0.0069	0.0197	0.0003	129.1	6.2	125.9	2.0

Table 1 (*continued*)

Sample	Concentration (ppm)			Th/U	Measured isotopic ratios						Ages (Ma)			
	U	Th	Pb		$^{207}Pb/^{206}Pb$	1σ	$^{207}Pb/^{235}U$	1σ	$^{206}Pb/^{238}U$	1σ	$^{207}Pb/^{235}U$	1σ	$^{206}Pb/^{238}U$	1σ
JS239-7	102	42	50.5	2.43	0.0481	0.0025	0.1270	0.0062	0.0193	0.0002	121.4	5.6	123.2	1.5
JS239-8	43	21	4.0	2.03	0.0502	0.0027	0.1362	0.0077	0.0197	0.0003	129.7	6.9	125.6	1.9
JS239-9	232	55	101.6	4.24	0.0502	0.0017	0.1371	0.0049	0.0198	0.0003	130.4	4.4	126.3	1.6
JS239-10	132	46	64.8	2.85	0.0502	0.0018	0.1379	0.0052	0.0199	0.0002	131.2	4.6	126.8	1.4
JS239-11	254	68	113.7	3.72	0.0504	0.0013	0.1349	0.0040	0.0194	0.0003	128.5	3.5	124.0	1.7
JS239-12	133	50	50.8	2.67	0.0495	0.0024	0.1309	0.0059	0.0193	0.0003	124.9	5.3	123.5	2.2
JS239-13	228	51	112.7	4.50	0.0514	0.0015	0.1367	0.0039	0.0195	0.0003	130.1	3.5	124.2	1.6
JS239-14	86	42	39.1	2.08	0.0512	0.0017	0.1407	0.0049	0.0199	0.0003	133.7	4.4	127.3	1.6
JS239-15	236	74	105.3	3.19	0.0505	0.0014	0.1326	0.0036	0.0191	0.0002	126.4	3.2	122.2	1.3
JS239-16	78	48	32.1	1.61	0.0511	0.0017	0.1381	0.0048	0.0196	0.0003	131.3	4.2	125.4	1.7

4. Results of ages

4.1. Zircon U–Pb LA-MC-ICP-MS data

The isotopic results for zircons analyzed in this study are summarized in Table 1. Typical CL images of zircon and $^{206}Pb/^{238}U$ vs. $^{207}Pb/^{235}U$ diagrams of zircon grains analyzed by LA-MC-ICP-MS are shown in Figs. 9 and 10, respectively.

Zircon grains from quartz monzonite sample JS520 from Yuhuasi are 50–130 μm long, with length/width ratios of 1–2. They are mostly euhedral, colorless, or pale white to gray, with excellent prism and pyramid faces and oscillatory zoning in CL images (Fig. 9a). These grains contain relatively low amounts of U (16–91 ppm) and Th (34–222 ppm), and yield Th/U ratios of 1.67–3.24, consistent with a magmatic origin (e.g., Hoskin and Black, 2000). Fourteen analyses of zircons yielded $^{206}Pb/^{238}U$ ages ranging from 127.1 ± 4.0 to 135.1 ± 10.2 Ma (Table 1) and a weighted mean $^{206}Pb/^{238}U$ age of 130.3 ± 1.5 Ma (n = 14, MSWD = 0.34, Fig. 10a).

Zircon grains from quartz diorite sample JS218 from Yuhuasi are 50–100 μm long, with length/width ratios of 1–2. They are mostly euhedral, colorless, and have excellent prism and pyramid

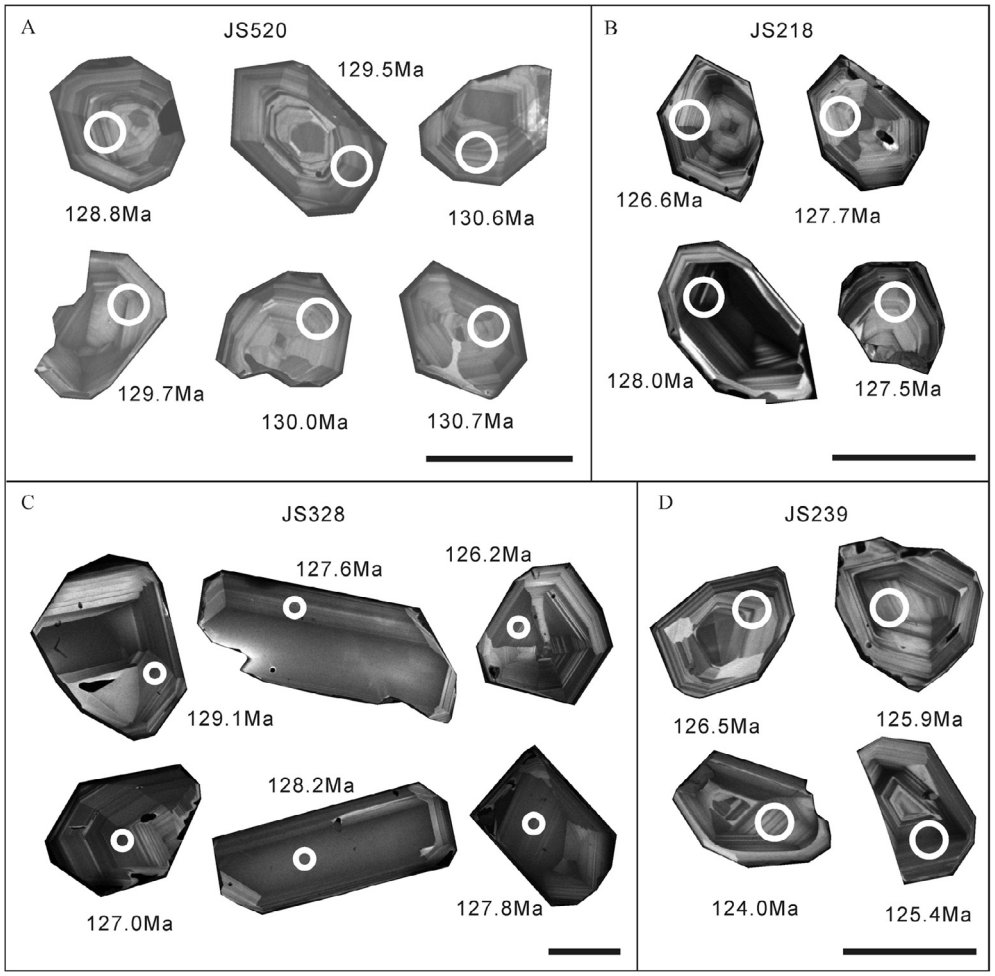

Fig. 9. Typical CL images of zircon and analyzed spots from each sample. (a) Quartz monzonite (sample JS520). (b) Quartz diorite (sample JS218). (c) Quartz diorite (sample JS328). (d) Quartz diorite porphyry dike (sample JS239). Scale in the figure is 100 μm.

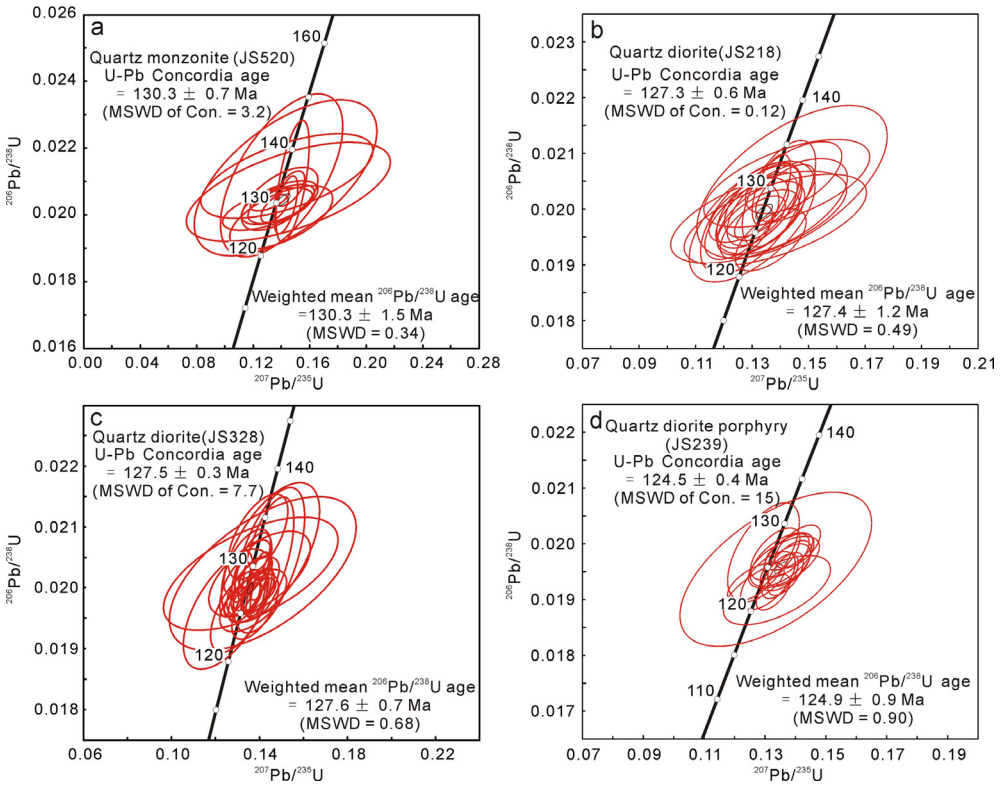

Fig. 10. $^{206}Pb/^{238}U$ vs. $^{207}Pb/^{235}U$ diagrams of zircon from the intrusion analyzed by LA-MC-ICP-MS, (a) Quartz monzonite (sample JS520). (b) Quartz diorite (sample JS218). (c) Quartz diorite (sample JS328). (d) Quartz diorite porphyry dike (sample JS239).

faces and oscillatory zoning in CL images (Fig. 9b). These grains contain relatively low amounts of U (18–69 ppm) and Th (33–325 ppm), and yield Th/U ratios of 1.85–4.74, indicating their magmatic origin. Twenty-one analyses of zircons yielded $^{206}Pb/^{238}U$ ages ranging from 124.2 ± 2.3 to 131.2 ± 2.7 Ma (Table 1) and a weighted mean $^{206}Pb/^{238}U$ age of 127.4 ± 1.2 Ma (n = 21, MSWD = 0.49, Fig. 10b).

Zircon grains from quartz diorite sample JS328 from Chenjiawan are 100–330 μm long, with length/width ratios of 2–4. They are mostly euhedral, colorless, or light yellow, with excellent prism and pyramid faces and oscillatory zoning in CL images (Fig. 9c). Apart from one analysis (spot JS328-24) with high contents of U (466 ppm) and Th (1081 ppm), and a Th/U ratio of 2.32, zircon grains from sample JS328 contain relatively low amounts of U (20–150 ppm) and Th (25–339 ppm), and yield Th/U ratios of 1.25–3.93, indicating a magmatic origin. Twenty-seven analyses of zircons yielded $^{206}Pb/^{238}U$ ages ranging from 125.2 ± 2.8 to 133.0 ± 2.9 Ma (Table 1) and a weighted mean $^{206}Pb/^{238}U$ age of 127.6 ± 0.7 Ma (n = 27, MSWD = 0.68, Fig. 10c).

Zircon grains from quartz diorite porphyry sample JS239 from Zhangfushan are 90–200 μm long, with length/width ratios of 1–2. They are mostly euhedral and colorless, with excellent prism and pyramid faces and oscillatory zoning in CL images (Fig. 9d). These grains contain relatively low amounts of U (21–74 ppm) and Th (43–254 ppm), and yield Th/U ratios of 1.61–4.50, indicating their magmatic origin. Sixteen analyses of zircons yielded $^{206}Pb/^{238}U$ ages ranging from 122.2 ± 1.3 to 127.3 ± 1.6 Ma (Table 1) and a weighted mean $^{206}Pb/^{238}U$ age of 124.9 ± 0.9 Ma (n = 16, MSWD = 0.90, Fig. 10d).

4.2. Titanite U–Pb LA-ICP-MS data

The isotopic results for titanite grains analyzed in this study are summarized in Table 2. Typical BSE and plane-polarized transmitted light images of titanite and $^{206}Pb/^{238}U$ vs. $^{207}Pb/^{235}U$ diagrams of titanite analyzed by LA-ICP-MS are shown in Figs. 11and 12, respectively.

Titanite grains from sample JS444 are euhedral, light to dark brown, with excellent wedge-shaped and singles twins and sector zoning in BSE images (Fig. 11a). The crystals are 5–10 mm long, with length/width ratios of 3–7. Apart from two analysis (spot JS444-9 and JS444-16) with relatively high contents of U (143 ppm and 212 ppm) and Th (682 ppm and 627 ppm), respectively, other titanite grains contain relatively low amounts of U (47–92 ppm) and Th (255–541 ppm), and yield Th/U ratios of 2.96–6.93. Twenty-five analyses of titanite grains yielded $^{206}Pb/^{238}U$ ages ranging from 127.0 ± 2.6 to 134.2 ± 2.9 Ma (Fig. 12a, Table 2) with a weighted mean $^{206}Pb/^{238}U$ age of 129.5 ± 1.2 Ma (n = 25, MSWD = 0.45, Fig. 12b).

Titanite grains from sample JS558 are euhedral, light to dark brown, with excellent wedge-shaped and sector zoning in BSE images (Fig. 11c). The crystals are 3–6 mm long, with length/width ratios of 2–5. Titanite grains contain relatively low amounts of U (24–126 ppm) and Th (349–1372 ppm), and have high Th/U ratios of 8.90–18.35. Twenty-eight analyses of titanite grains yielded $^{206}Pb/^{238}U$ ages ranging from 124.2 ± 3.6 to 134.8 ± 3.5 Ma (Fig. 12c, Table 2) with a weighted mean $^{206}Pb/^{238}U$ age of 130.7 ± 1.2 Ma (n = 28, MSWD = 0.62, Fig. 12d).

4.3. Phlogopite $^{40}Ar/^{39}Ar$ data

The $^{40}Ar/^{39}Ar$ data for phlogopite samples are listed in Table 3 and graphically illustrated in Fig. 13. The argon release spectrum for phlogopite from sample D10-3 from the Kejiashan deposit shows a convex pattern over the first 15.3% of ^{39}Ar released, which is followed by a plateau comprising 84.7% of the released gas and yielding a well-defined plateau age of 127.6 ± 0.9 Ma (MSWD = 0.43, Fig. 13a, Table 3). The inverse isochron age calcu-

Table 2
LA-ICPMS U-Pb isotope data for titanite from the Jinshandian ore field.

Sample	Concentration (ppm)				Th/U	Measured isotopic ratios								^{207}Pb-corrected ages (Ma)	
	U	Th	Pb	Zr		^{207}Pb/^{206}Pb	1σ	^{207}Pb/^{235}U	1σ	^{206}Pb/^{238}U	1σ	^{208}Pb/^{232}U	1σ	^{206}Pb/^{238}U	1σ
JS444-1	58	382	3.2	419	6.59	0.04539	0.0038	0.12696	0.01041	0.02029	0.00047	0.00685	0.00013	130.0	3.1
JS444-2	55	288	3.1	101	5.26	0.05769	0.00768	0.16504	0.02117	0.02075	0.00082	0.0075	0.00022	130.9	5.3
JS444-3	68	406	3.5	322	5.98	0.05684	0.00383	0.16306	0.01067	0.02081	0.00048	0.00677	0.00013	131.4	3.1
JS444-4	70	395	3.5	372	5.65	0.06649	0.00349	0.18954	0.00947	0.02068	0.00047	0.00681	0.00013	129.0	3.0
JS444-5	80	541	4.4	1241	6.73	0.05373	0.00376	0.15108	0.01016	0.02039	0.00052	0.00667	0.00013	129.3	3.3
JS444-6	52	266	2.5	246	5.15	0.07333	0.00425	0.21005	0.01163	0.02078	0.0005	0.007	0.00014	128.5	3.2
JS444-7	65	390	3.4	368	5.96	0.04539	0.00326	0.13113	0.00924	0.02095	0.00044	0.0067	0.00012	134.2	2.9
JS444-8	66	368	3.2	513	5.55	0.07021	0.00367	0.19595	0.0098	0.02024	0.00045	0.00657	0.00012	125.7	2.8
JS444-9	143	682	6.6	1791	4.79	0.07714	0.002	0.22208	0.00542	0.02088	0.00038	0.00679	0.00012	128.5	2.4
JS444-10	59	304	2.9	590	5.16	0.05969	0.00389	0.17083	0.01076	0.02076	0.00049	0.00675	0.00014	130.6	3.1
JS444-11	56	321	2.7	1104	5.78	0.04259	0.00431	0.11979	0.01193	0.0204	0.0005	0.00663	0.00013	131.2	3.3
JS444-12	60	379	3.2	399	6.32	0.05995	0.00378	0.16845	0.01033	0.02038	0.00045	0.00653	0.00012	128.2	2.9
JS444-13	67	398	3.4	456	5.92	0.0517	0.00348	0.14575	0.00959	0.02045	0.00044	0.00654	0.00012	130.0	2.8
JS444-14	48	256	2.4	377	5.29	0.07328	0.0041	0.2083	0.01116	0.02062	0.00047	0.00689	0.00014	127.5	3.0
JS444-15	212	627	7.3	691	2.96	0.04944	0.00133	0.14013	0.00366	0.02056	0.00036	0.00664	0.00011	131.1	2.3
JS444-16	63	339	3.0	364	5.35	0.05662	0.00372	0.16287	0.01039	0.02086	0.00047	0.00674	0.00013	131.8	3.0
JS444-17	55	299	2.6	321	5.47	0.07187	0.004	0.20399	0.01095	0.02058	0.00046	0.00661	0.00013	127.5	2.9
JS444-18	92	442	4.1	805	4.80	0.05332	0.0023	0.15277	0.0064	0.02078	0.0004	0.00655	0.00012	131.8	2.5
JS444-19	56	312	2.7	646	5.53	0.0516	0.00404	0.14576	0.01113	0.02049	0.00048	0.00669	0.00013	130.3	3.1
JS444-20	52	263	2.4	340	5.09	0.07576	0.00458	0.21597	0.01249	0.02067	0.0005	0.00641	0.00014	127.4	3.2
JS444-21	73	506	4.1	670	6.93	0.07569	0.00298	0.215	0.00807	0.0206	0.00042	0.00659	0.00012	127.0	2.6
JS444-22	49	300	2.6	340	6.07	0.05472	0.00424	0.15506	0.01179	0.02055	0.00046	0.00658	0.00013	130.1	3.0
JS444-23	47	255	2.1	267	5.44	0.04497	0.00689	0.12638	0.01896	0.02038	0.00074	0.00672	0.00019	130.7	4.8
JS444-24	61	365	3.1	409	5.94	0.0575	0.00354	0.16081	0.00967	0.02029	0.00043	0.00648	0.00012	128.1	2.8
JS444-25	57	296	2.7	433	5.22	0.05454	0.00351	0.15205	0.00955	0.02022	0.00044	0.00676	0.00013	128.1	2.8
JS558-1	75	1243	8.0	57	16.54	0.03827	0.00304	0.10594	0.00829	0.02008	0.00042	0.00666	0.00011	129.8	2.7
JS558-2	29	436	3.1	99	15.01	0.07443	0.00723	0.21343	0.01984	0.0208	0.00069	0.00697	0.00014	128.4	4.4
JS558-3	55	488	3.8	343	8.90	0.05895	0.00336	0.17033	0.0094	0.02095	0.00046	0.00718	0.00013	131.9	2.9
JS558-4	33	496	3.4	41	14.95	0.04929	0.00432	0.14176	0.01214	0.02086	0.00052	0.00688	0.00012	133.0	3.4
JS558-5	39	725	4.8	352	18.35	0.03686	0.00563	0.10582	0.01586	0.02082	0.00073	0.00679	0.00014	134.8	4.8
JS558-6	70	927	6.5	504	13.28	0.05506	0.00375	0.16168	0.01059	0.0213	0.00054	0.00693	0.00013	134.8	3.5
JS558-7	99	951	7.7	755	9.60	0.05802	0.00201	0.16593	0.00554	0.02074	0.00040	0.00665	0.00011	130.8	2.5
JS558-8	25	401	2.8	108	15.95	0.07096	0.00601	0.20549	0.01686	0.021	0.00057	0.00693	0.00012	130.3	3.7
JS558-9	53	848	5.7	49	16.05	0.04999	0.00341	0.14309	0.00954	0.02076	0.00046	0.00684	0.00012	132.2	3.0
JS558-10	23	349	2.4	18	14.88	0.07946	0.00748	0.22265	0.02011	0.02032	0.00064	0.00708	0.00013	124.7	4.1
JS558-11	38	694	4.5	358	18.04	0.06052	0.00417	0.17329	0.01162	0.02077	0.00048	0.0066	0.00011	130.6	3.1
JS558-12	85	1056	7.1	74	12.43	0.05745	0.00235	0.1614	0.00635	0.02038	0.00041	0.00657	0.00011	128.6	2.6
JS558-13	52	805	5.4	145	15.52	0.03832	0.00361	0.10853	0.01009	0.02054	0.00046	0.00688	0.00012	132.8	3.0
JS558-14	27	437	3.0	177	16.01	0.08187	0.00611	0.22909	0.01635	0.0203	0.00056	0.00695	0.00012	124.2	3.6
JS558-15	126	1372	9.6	203	10.86	0.05003	0.00172	0.14248	0.00466	0.02066	0.00040	0.00656	0.00011	131.6	2.5
JS558-16	32	525	3.4	119	16.29	0.03767	0.00487	0.10793	0.0138	0.02078	0.00052	0.00659	0.00012	134.4	3.4
JS558-17	27	425	2.9	40	15.88	0.06857	0.00661	0.19739	0.01821	0.02088	0.00069	0.00684	0.00013	129.9	4.4
JS558-18	39	587	3.9	42	14.96	0.04011	0.00484	0.11371	0.01354	0.02056	0.00053	0.00666	0.00012	132.6	3.5
JS558-19	30	494	3.3	135	16.33	0.03761	0.00527	0.10508	0.01459	0.02026	0.00052	0.00685	0.00012	131.1	3.4
JS558-20	61	885	5.9	24	14.60	0.06132	0.0031	0.17007	0.0083	0.02011	0.00043	0.00675	0.00011	126.3	2.7
JS558-21	30	463	3.1	92	15.39	0.04857	0.00525	0.14054	0.01494	0.02099	0.00055	0.00673	0.00012	133.9	3.6
JS558-22	40	463	3.3	47	11.70	0.06595	0.00404	0.18849	0.01114	0.02073	0.00048	0.00682	0.00012	129.4	3.1
JS558-23	81	1181	8.0	288	14.63	0.0555	0.00229	0.15898	0.00631	0.02077	0.00042	0.00679	0.00011	131.4	2.7
JS558-24	90	1056	7.4	25	11.78	0.04956	0.00212	0.14105	0.00588	0.02064	0.00040	0.0067	0.00011	131.6	2.6
JS558-25	48	721	4.6	120	14.95	0.03595	0.00404	0.10042	0.01116	0.02026	0.00048	0.00662	0.00012	131.3	3.2
JS558-26	43	685	4.5	147	16.04	0.06609	0.00393	0.18637	0.01074	0.02045	0.00046	0.00669	0.00011	127.7	2.9
JS558-27	68	975	6.3	137	14.40	0.06028	0.00256	0.17315	0.0071	0.02083	0.00042	0.00634	0.00011	131.0	2.7
JS558-28	78	882	6.4	80	11.30	0.05275	0.00271	0.15114	0.00739	0.02078	0.00048	0.00655	0.00012	131.9	3.1

lated on the same plateau steps is 128.6 ± 1.5 Ma (MSWD = 13, ^{40}Ar/^{36}Ar ratio: 258 ± 60, Fig. 13b), which is indistinguishable from the plateau age. Nevertheless, the inverse isochron age is preferred because the atmospheric values are slightly decreased and this might indicate slight argon loss occurred in the sample (Kuiper, 2002).

Sample D9-1 from the Zhangjingjian deposit shows Ar loss in the low temperature steps, perhaps from grain margins, but yields a well-defined plateau age at 119.4 ± 0.9 Ma (MSWD = 1.15, Fig. 13c, Table 3). The plateau consists of eight consecutive steps accounting for 97.5% of the total ^{39}Ar released. The inverse isochron age calculated for the same plateau steps is 118.3 ± 5.2 Ma (MSWD = 21, ^{40}Ar/^{36}Ar ratio: 322 ± 190), which is indistinguishable from the plateau age (Fig. 13d). Characteristics of the spectrum suggest that a minor amount of excess argon was present in the sample. Therefore, the inverse isochron age is again preferred because the atmospheric values are slightly increased, which might indicate that the plateau overestimated the mineralization age (Kuiper, 2002; Deckart et al., 2014).

5. Discussion

5.1. Geochronological framework of the Jinshandian ore field

The Jinshandian pluton consists mainly of quartz diorite and quartz monzonite, as well as quartz diorite porphyry dikes. Potassium–Ar dating of whole rock samples yielded an age of 132 Ma for the quartz monzonite and 142 Ma for the quartz diorite, respectively (cf. Shu et al., 1992). Additionally, K–Ar and Rb–Sr analyses

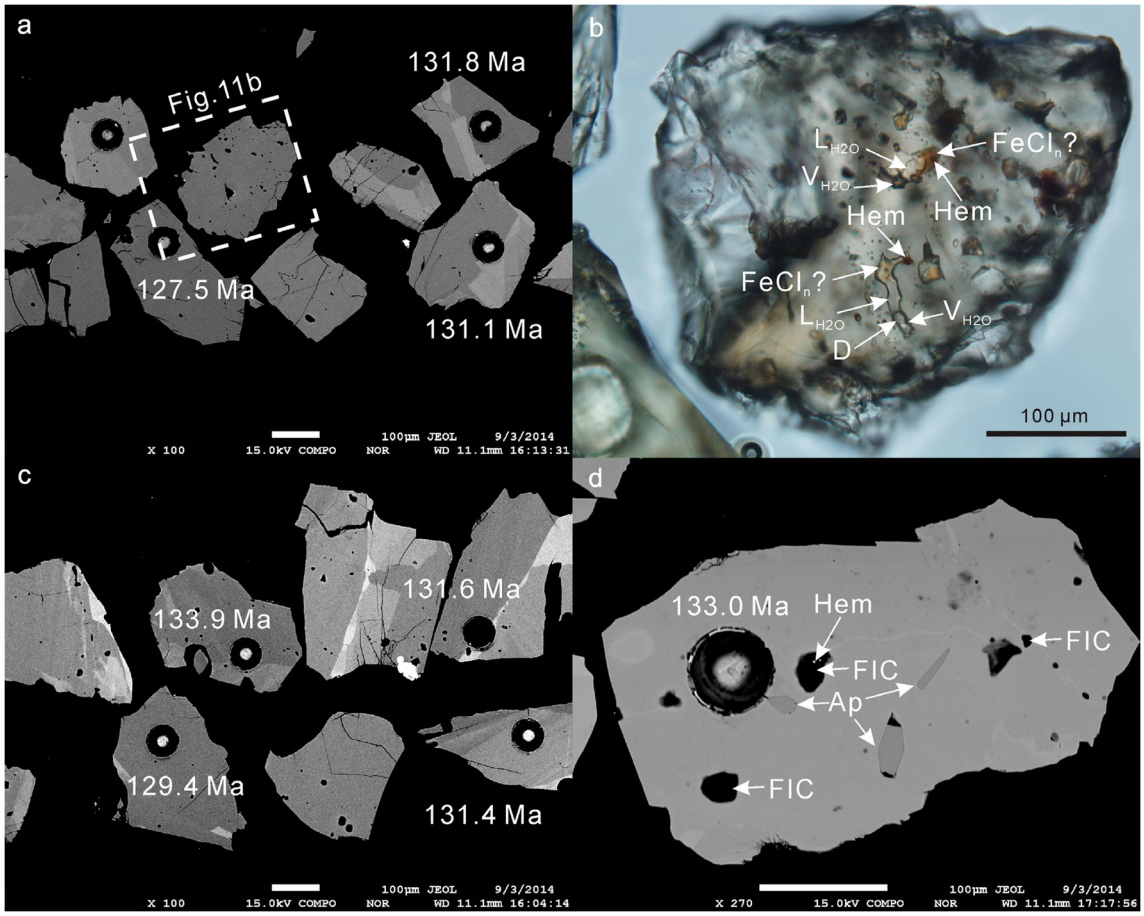

Fig. 11. BSE and photomicrograph images of hydrothermal titanite from the samples analyzed by LA-ICP-MS. $^{206}Pb/^{238}U$ ages are indicated in the image where analyses were done. (a) Titanite in scapolite + diopside skarn (sample JS444). (b) Fluid inclusions of titanite include hematite, $FeCl_n$?, and other transparent daughter minerals. (c) Titanite in pyrite + anhydrite + chlorite + apatite + titanite + calcite metasomatic rock (sample JS558). (d) Apatite grain, primary and secondary fluid inclusion holes and holes with hematite inside can also be recognized in the titanite. (a, c and d) Backscattered electron images. (b) Plane-polarized transmitted light. (*Abbreviations:* Ap–apatite, D–daughter mineral, FIH–fluid inclusion hole, Hem–hematite.)

for phlogopite from the No. I orebody of the Zhangfushan deposit yielded ages of 117 and 128 Ma, respectively (cf. Shu et al., 1992). Compared to the K–Ar and Rb–Sr dating methods, the U–Pb zircon geochronometer is remarkably robust and little affected by the subsequent events (McDougall and Harrison, 1999). The sample of quartz monzonite yielded a weighted mean $^{206}Pb/^{238}U$ age of 130.3 ± 1.5 Ma (JS520, n = 14, MSWD = 0.34) (Fig. 9a). This age overlaps within error those of the zircon grains (133–127 Ma) from quartz diorite, diorite, and granite of the Jinshandian pluton (Li et al., 2009; Xie et al., 2011b; Qu et al., 2012). Two quartz diorite samples yielded weighted mean $^{206}Pb/^{238}U$ ages of 127.4 ± 1.2 Ma (JS218, n = 21, MSWD = 0.49) and 127.6 ± 0.7 Ma (JS328, n = 27, MSWD = 0.68), respectively (Fig. 9b, c). The robustness of the U–Pb zircon ages demonstrates that the quartz monzonite and quartz diorite in the Jinshandian ore field were emplaced at 130 Ma and 128 Ma, respectively.

As shown in the Fig. 8, the titanite grains replaced scapolite and diopside (Fig. 8a, b), and in turn were replaced by hydrothermal minerals (Fe–Ti oxide, anhydrite, and pyrite: Fig. 8c, d, e, f). The primary and secondary fluid inclusions (Fig. 10b, d), as well as apatite and diopside mineral inclusions (Fig. 10d), indicate that the titanite grains are of unequivocal hydrothermal origin. The formation temperature of titanite was estimated at 573–707 °C for sample JS444 and 509–663 °C for sample JS558 (assuming P = 0.05 Gpa, a_{TiO2} = - a_{SiO2} = 0.5: Hayden et al., 2008). The temperature ranges overlap with the closure temperature for the Pb isotope systems in titanite (cf. Spencer et al., 2013), suggesting that the U–Pb system in these titanite grains may have remained closed after their crystallization. Mineral assemblages and crosscutting relationships (Fig. 8a, d) suggest titanite formed during the early mineralization stage. In addition, decrepitation temperatures for fluid inclusions in magnetite from the Zhangfushan deposit range from 350 °C to 560 °C (Shu et al., 1992). Thus the closure temperatures of the U–Pb for hydrothermal titanite at Zhangfushan were higher than the formation temperature of the magnetite. Based on the above considerations, the two well-defined weighted mean $^{206}Pb/^{238}U$ ages of titanite (JS444, 129.5 ± 1.2 Ma, n = 25, MSWD = 0.45, and JS558, 130.7 ± 1.2 Ma, n = 28, MSWD = 0.62) are interpreted as the age of hydrothermal activity and the maximum age for magnetite mineralization.

The calculations and experimental diffusion studies indicate that the closure temperature of the $^{40}Ar/^{39}Ar$ system in phlogopite is between 250 °C and 350 °C (McDougall and Harrison, 1999). Therefore, $^{40}Ar/^{39}Ar$ ages measured for hydrothermal phlogopite have been widely used for direct dating of magmatic-hydrothermal ore deposits (Mao et al., 2006; Xie et al., 2012; Chiaradia et al., 2013). Two phlogopite samples in this study yield consistent plateau and inverse isochron ages, and they overlap within error, indicating the reliability of the data for defining the crystallization age of phlogopite. Phlogopite in sample D10-3 coexists with magnetite, and its closure temperature within the argon isotope system is slightly lower than the fluid inclusion decrepitation temperatures of the magnetite (350 °C–560 °C, Shu et al., 1992). Therefore, the $^{40}Ar/^{39}Ar$ age can be further interpreted as the minimum age of magnetite

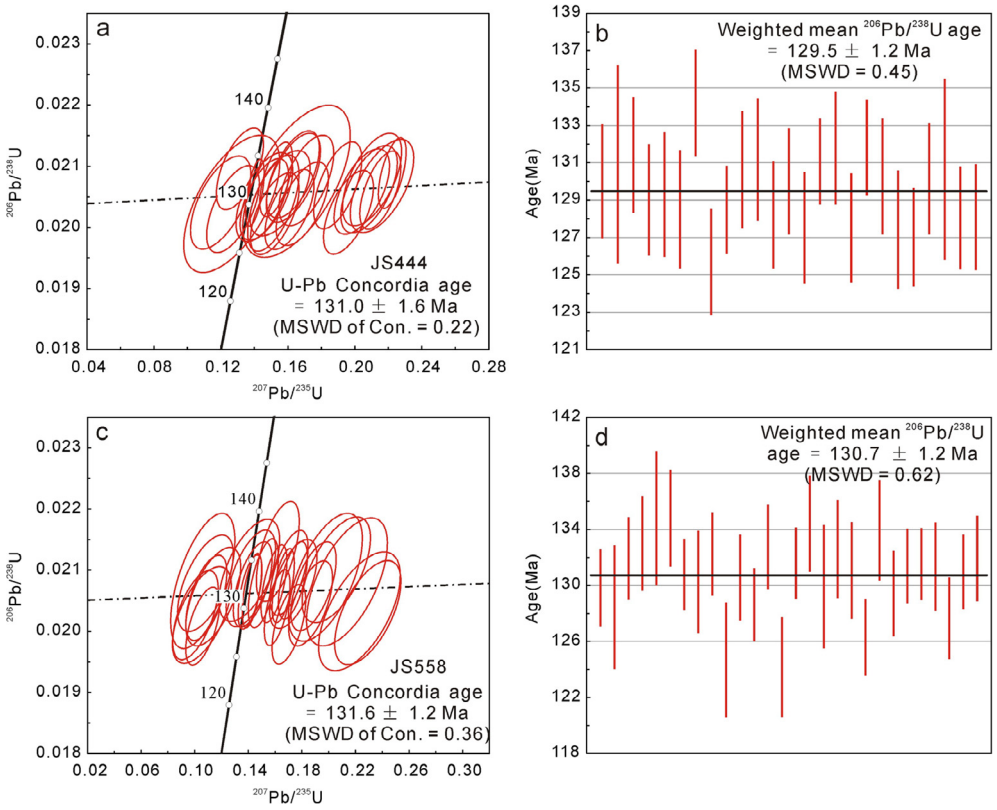

Fig. 12. $^{206}Pb/^{238}U$ vs. $^{207}Pb/^{235}U$ and weighted mean $^{206}Pb/^{238}U$ age diagrams of hydrothermal titanite from the Zhangfushan deposit analyzed by LA-ICP-MS. (a) Titanite in scapolite + diopside skarn (sample JS444). (b) Titanite in pyrite + anhydrite + chlorite + apatite + titanite + calcite metasomatic rock (sample JS558).

Table 3
$^{40}Ar/^{39}Ar$ isotope data for phlogopite from the Jinshandian ore field.

Step	T(°C)	$(^{40}Ar/^{39}Ar)_m$	$(^{36}Ar/^{39}Ar)_m$	$(^{37}Ar_0/^{39}Ar)_m$	$(^{38}Ar/^{39}Ar)_m$	^{40}Ar (%)	$^{40}Ar^*/^{39}Ar$	^{39}Ar ($\times10^{-14}$ mol)	^{39}Ar(Cum.) (%)	Age (Ma)	±1σ (Ma)
Sample: D10-3, W = 29.01 mg, J = 0.002814											
1	700	227.2888	0.6602	0.0000	0.1372	14.16	32.1805	0.01	0.05	156.0	96.0
2	780	109.1313	0.3542	0.0000	0.085	4.09	4.4609	0.28	1.42	22.5	3.8
3	820	126.4704	0.3626	0.0000	0.0852	15.27	19.3108	0.07	1.79	95.5	10.6
4	870	46.5414	0.1277	0.0000	0.0282	18.89	8.7895	0.23	2.92	140.0	4.4
5	920	42.3429	0.0379	0.0000	0.0206	73.54	31.1380	0.35	4.64	151.5	3.6
6	960	28.8550	0.0072	0.0000	0.016	92.63	26.7292	2.18	15.31	130.8	2.6
7	990	27.0312	0.0026	0.0000	0.0151	97.17	26.2653	3.01	30.07	128.6	2.4
8	1020	26.7973	0.0021	0.0000	0.0154	97.67	26.1739	5.15	55.35	128.2	2.4
9	1060	27.3585	0.0037	0.0000	0.0157	95.95	26.2508	3.57	72.87	128.6	2.4
10	1100	27.8272	0.0061	0.0000	0.0157	93.47	26.0090	1.75	81.45	127.4	2.4
11	1150	27.3967	0.0049	0.0000	0.0158	94.74	25.9558	2.15	91.98	127.2	2.4
12	1200	27.0290	0.0038	0.0000	0.0158	95.85	25.9060	1.13	97.52	126.9	2.6
13	1280	28.6608	0.0098	0.0000	0.0182	89.91	25.7685	0.33	99.14	126.3	2.8
14	1400	30.9879	0.0174	0.0000	0.0210	83.43	25.8523	0.17	100.00	126.7	5.4
Sample: D9-1, W = 28.06 mg, J = 0.002864											
1	700	124.2364	0.1206	0.0000	0.0526	71.32	88.6065	0.01	0.09	408.0	78.0
2	800	124.3118	0.3615	2.5335	0.0503	14.20	17.6915	0.03	0.34	89.0	30.0
3	870	98.6081	0.2864	0.3692	0.0911	14.19	14.0001	0.04	0.72	71.0	22.0
4	920	72.7644	0.1727	0.0000	0.0691	29.88	21.7400	0.05	1.26	109.0	13.8
5	960	50.3316	0.0981	0.0688	0.0365	42.42	21.3499	0.13	2.53	107.1	5.6
6	990	29.2332	0.0186	0.0000	0.0156	81.17	23.7283	0.22	4.69	118.6	4.6
7	1020	26.9000	0.0121	0.0542	0.0191	86.72	23.3286	0.36	8.17	116.7	2.8
8	1060	26.4905	0.0085	0.0135	0.0196	90.51	23.9756	0.55	13.54	119.8	2.6
9	1100	25.9751	0.0063	0.0586	0.0155	92.87	24.1233	0.97	22.98	120.5	2.4
10	1150	25.5739	0.0059	0.0185	0.0163	93.18	23.8308	1.52	37.75	119.1	2.4
11	1200	25.2402	0.0047	0.0000	0.015	94.48	23.8481	1.78	55.06	119.2	2.4
12	1280	25.6429	0.0046	0.0000	0.0141	94.70	24.2831	2.33	77.73	121.3	2.4
13	1400	25.2524	0.0053	0	0.0147	93.77	23.6797	2.29	100.00	118.4	2.4

* Radiogenic origin.

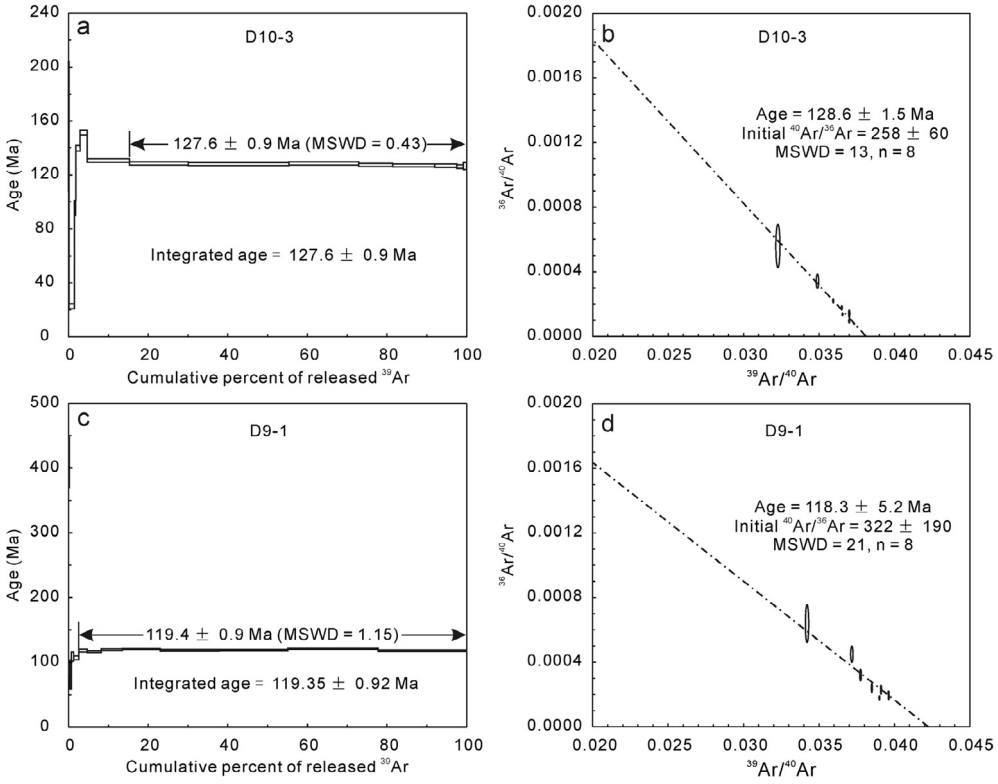

Fig. 13. Plateau and inverse isochron $^{40}Ar/^{39}Ar$ ages of hydrothermal phlogopite from the Kejiashan (a, b) and Zhangjingjian (c, d) deposits.

mineralization. The phlogopite $^{40}Ar/^{39}Ar$ age (128.6 ± 1.5 Ma) for sample D10-3 is slightly younger than the titanite U–Pb ages (JS444, 129.5 ± 1.2 Ma, and JS558, 130.7 ± 1.2 Ma), which is consistent with our determined paragenetic sequence (Fig. 5). These ages indicate that the Fe deposits within the Jinshandian ore field formed at 130–128 Ma, which is in excellent agreement with the LA-ICP-MS zircon U–Pb ages for the Jinshandian pluton (133–127 Ma). These ages confirm a genetic linkage between the Jinshandian intrusion and adjacent Fe skarn deposits. Sample D9-1 from the phlogopite vein that cuts the massive magnetite probably represents a discrete later hydrothermal event and is discussed below.

The post-ore quartz diorite porphyry dike yielded a weighted mean $^{206}Pb/^{238}U$ age of 124.9 ± 0.9 Ma (JS239, n = 16, MSWD = 0.90) (Fig. 9d). This age is comparable to that of the youngest volcanic rock (basaltic andesite, SHRIMP zircon U–Pb age, 125 ± 2 Ma, Xie et al., 2011a) in the Jinniu basin. Furthermore, Yao et al. (2015) dated a porphyritic diabase dike that crosscuts the magnetite orebody in the Chengchao Fe skarn deposit of the Edong district (Fig. 2) by LA-ICP-MS U–Pb zircon at 126 ± 1 Ma. These two ages overlap within error, which confirms the reliability of the age of the quartz diorite porphyry dike, indicating the dike probably represents the end of extensive magmatic activity at Jinshandian.

The zoning of the skarn alteration, the distribution of Fe mineralization, and the dates obtained for the magmatic and hydrothermal minerals all indicate that hydrothermal fluids are genetically associated with the quartz monzonite and quartz diorite. The U–Pb zircon ages for the igneous rocks of the Jinshandian pluton overlap within error the ages of the hydrothermal titanite and phlogopite (D10-3).

5.2. 122–118 Ma episode of magmatic-hydrothermal activity in the Edong district

Obvious differences between petrology, geochemistry, and geochronology of intrusions, as well as features of the related ore deposits themselves, imply two episodes of late Mesozoic magmatism and associated Fe skarn formation in the Edong district (e.g., Li et al., 2009, 2010; Xie et al., 2011c, 2012, 2013; Huang et al., 2013; Yao et al., 2015). The first is represented by the 140–136 Ma diorites and quartz diorites, and the magmatism is associated with 141–137 Ma Fe–Cu or Cu–Fe (–Au) skarn deposits (Tieshan and Tonglushan) (Fig. 2). Subsequently, emplacement of 133–127 Ma quartz diorites and granites is associated with 133–129 Ma Fe skarn deposit formation at Zhangfushan and Chengchao. The new zircon U–Pb ages for the Jinshandian pluton and hydrothermal titanite U–Pb and phlogopite $^{40}Ar/^{39}Ar$ ages in this study are consistent (within error) with the second magmatic-hydrothermal event occurring in the Edong district.

Phlogopite sample D9-1 yields a reliable $^{40}Ar/^{39}Ar$ age of 118.3 ± 5.2 Ma, but is much younger than other ages in this and previous studies (Table 3, Fig. 12). However, this age might be meaningful if one takes the age of magmatic-hydrothermal activity of the entire Edong district into consideration. Li et al. (2009) reported a 121.5 ± 0.5 Ma LA-ICP-MS U–Pb zircon age for a gabbro-diorite porphyry dike near the Wangbaoshan pluton (Fig. 2b). Xie and Mao (2008) also obtained a zircon SHRIMP U–Pb age of 121.2 ± 3.1 Ma for granite from the Echeng pluton (Fig. 2a). Li et al. (2010) published a magmatic titanite LA-ICP-MS U–Pb age of 120.6 ± 2.3 Ma from an albitite dike that intrudes both the quartz diorite and skarn, and an age of 121.5 ± 1.3 Ma for hydrothermal titanite in a calcite vein that cuts the skarn orebody (Fig. 2a). Qu et al. (2012) also reported a zircon LA-ICP-MS U–Pb age of 118.9 ± 1.2 Ma for quartz diorite from the Tieshan pluton (Fig. 2a). In addition, subhedral magnetite and pyrite grains filling spaces between coarse grains of phlogopite in sample D9-1 are partly replaced, and the fact that phlogopite veins crosscut the massive ore (Fig. 8l) confirms two episodes of hydrothermal activity. The results from different dating methods of various magmatic or hydrothermal minerals from different locations in the Edong district, coupled with crosscutting relationships, indicate a relatively young 122–118 Ma magmatic-hydrothermal event did occur

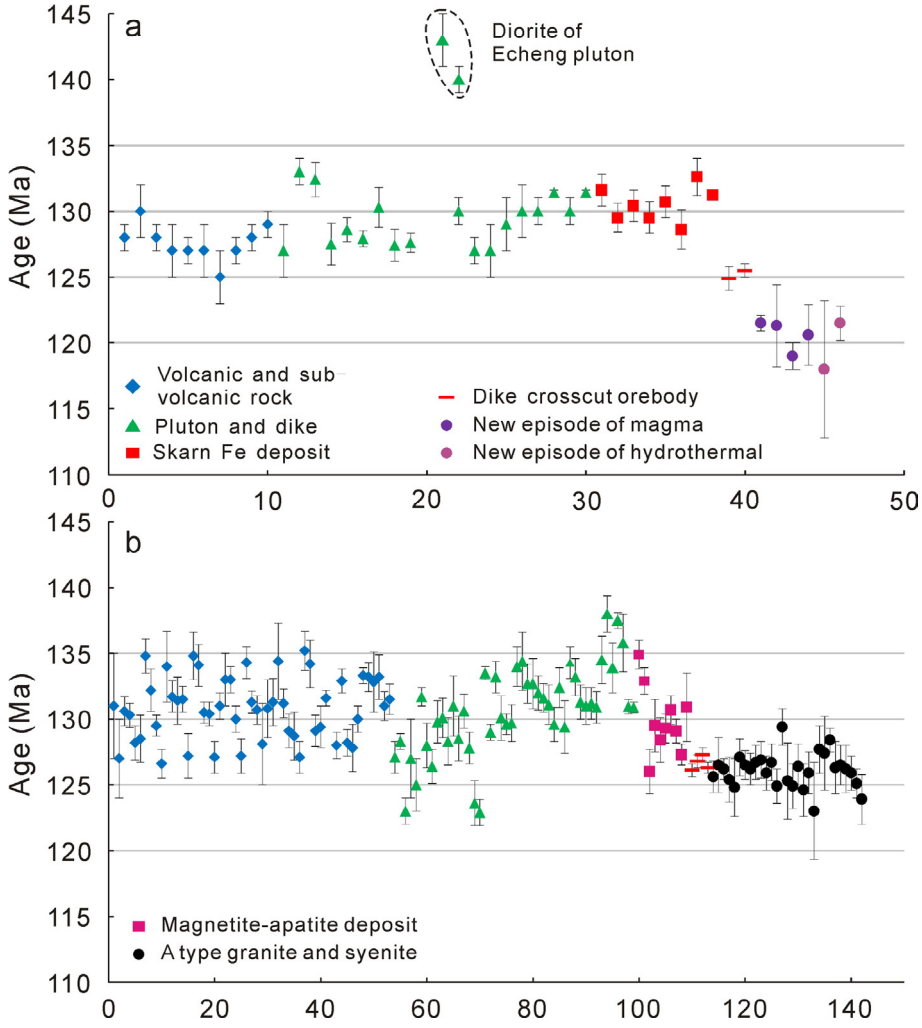

Fig. 14. Age distributions for the magmatic-hydrothermal event in the Edong district (a) and eastern part of the MLYRB (mainly from Ningwu and Luzong district) (b) after 135 Ma. (a) Data for Edong district are collated from Li et al. (2009, 2010), Xie et al. (2011c, 2012, 2013) and Yao et al. (2015) and references therein. (b) Data of eastern part of the MLYRB are collated from Zhang et al. (2003), Yan et al. (2009), Ma et al. (2010), Yuan et al. (2010a,b), Fan et al. (2011, 2014), Zhou et al. (2008b, 2010, 2011a,b, 2012) and Wang et al. (2014) and references therein.

in the Edong district (Fig. 14a). Thus, at least two episodes of hydrothermal events are represented in the Jinshandian ore field. The first episode was of great importance for Fe skarn deposit formation, whereas the extent and metallogenic significance of the second hydrothermal event is unclear.

5.3. Comparison between Fe skarn and magnetite-apatite deposits

Magnetite-apatite deposits represent one of the two major types of Fe deposit formed along the MLYRB after 135 Ma, and almost all such deposits are present in the Cretaceous Luzong and Ningwu terrigenous volcanic basins within the eastern part of the MLYRB (Mao et al., 2011). These deposits are genetically related to Early Cretaceous subvolcanic dioritic intrusions. The iron orebodies are developed along the contact between the intrusions and volcano-sedimentary rocks or occur in the apical zones of the intrusions. The mineralization and alteration phases can be divided into an early anhydrous silicate assemblage, a retrograde alteration assemblage, and a late argillic-carbonate alteration (Ningwu Research Group, 1978). The anhydrous silicate alteration is dominated by pyroxene and garnet with extensive albitization. The retrograde alteration zones are composed of hydrous silicates, such as actinolite, epidote, chlorite, phlogopite, albite, K-feldspar, and anhydrite. Magnetite is a dominant mineral deposited during the retrograde alteration stage, overprinting the early alteration stage. The late argillic-carbonate alteration is dominated by quartz, clays, carbonates, anhydrite, and alunite; some magnetite has been altered by hematite during this stage (Mao et al., 2006). Medium- to large-scale (14–64 Mt reserves) anhydrite/gypsum deposits are associated with or located near these deposits (Fig. 1, Mao et al., 2012; Li et al., 2014b; Zhou et al., 2014). Most anhydrite and sulfides deposited during the main mineralization stage within the magnetite-apatite deposits are enriched in the heavy sulfur isotope, with $\delta^{34}S$ ranging from +15.5‰ to +19.3‰ and +1.7‰ to +12.1‰, respectively (Zhang, 1986; Li et al., 2015). This feature indicates that the hydrothermal system experienced a significant incursion of exotic sulfur that might have been derived from the Middle Triassic evaporites bearing carbonate (Zhang, 1986; Li et al., 2014b, 2015). Hydrothermal micas from these deposits have $^{40}Ar/^{39}Ar$ plateau ages ranging from 134–128 Ma (Fig. 14b, Ma et al., 2010; Yuan et al., 2010b; Fan et al., 2011, 2014; Zhou et al., 2012). These ages are consistent with both 134–128 Ma zircon U–Pb ages for mineralization-related intrusions and 134–126 Ma ages of volcanic rocks (Fig. 14b, Zhang et al., 2003; Zhou et al., 2008b, 2010, 2011a; Yan et al., 2009; Yuan et al., 2010a; Wang et al., 2014 and references therein).

Post-ore granitic stocks in the Ningwu district have zircon U–Pb ages ranging from 127 to 126 Ma (Duan et al., 2012), indicating the magnetite-apatite ores in the MLYRB were formed no later than 127–123 Ma (Fan et al., 2008; Zhou et al., 2010; Yan et al., 2012).

The Fe-only skarn deposits in the Edong district in the western part of the MLYRB share similar prograde anhydrous and retrograde hydrous mineral assemblages, and magnetite is a dominant mineral during the retrograde stage (Yao et al., 2015; Zhu et al., 2015). These deposits are characterized by association with anhydrite/gypsum deposits with 2–45 Mt reserves, and hydrothermal anhydrite and pyrite deposited during the retrograde stage of Fe-skarn formation have heavy $\delta^{34}S$ values (anhydrite: +18.9‰ to +30.8‰; pyrite: +10.3‰ to +20.0‰; Xie et al., 2015; Zhu et al., 2015). These features are similar to those of the magnetite-apatite deposits in the Cretaceous basins along the eastern part of the MLYRB. Indeed, skarn mineral assemblages were developed in many of the magnetite-apatite deposits (e.g., Meishan, Washan, and Gushan), and these deposits are considered to be skarn-like (Mao et al., 2012) or also Fe skarn deposits (Meinert et al., 2005). Moreover, Mao et al. (2011) assigned the Zhangfushan and Chengchao deposits of the Edong district to the magnetite-apatite ore deposit family, indicating the affinity of these Fe-only skarn deposits with the magnetite-apatite deposits in the Cretaceous basins along the eastern part of the MLYRB.

The Fe-only skarn deposits occur mainly in the Jinshandian ore field and to the south of the Echeng pluton (Chengchao) in the Edong district. Ages of Fe mineralization range from 131 to 127 Ma based upon hydrothermal titanite and phlogopite ages and as indirectly constrained by dikes that crosscut the orebody dated at 124 Ma (Xie et al., 2012; Yao et al., 2015, and this study). These dates are almost coincident with those for 133–127 Ma granitoids and 130–125 Ma volcanic and subvolcanic rocks in the Jinniu basin (Xie et al., 2006, 2011a; Li et al., 2012) (Fig. 2a). A dataset of ages for magmatic-hydrothermal activity in the Edong district younger than 135 Ma can be compiled from data in this study and those of previous workers (Fig. 14). The volcanic and subvolcanic rocks, intrusive rocks, and deposits yield an older age mode of ca. 130 Ma (except for two ages of the diorite at the Echeng pluton) and a younger age mode of ca. 120 Ma. These correspond to the two episodes of magmatic-hydrothermal activity in the Edong district after 135 Ma and are separated by ca. ~10 m.y. (Fig. 13a). Two distinct ages for magmatic-hydrothermal events after 135 Ma in the eastern part of the MLYRB were also obtained in the same manner (Fig. 13b), with the volcanic and subvolcanic rocks, plutons, and deposits yielding an older age of ca. 130 Ma and the A-type granite and syenite yielding a younger age of ca. 126 Ma. The former one is in excellent agreement with the older age in the Edong district, indicating a similar magmatic-hydrothermal event within the eastern (Edong district) and western (Ningwu district) parts of the MLYRB (Mao et al., 2011). However, magmatic-hydrothermal activity in the MLYRB seems decoupled after ca. 126 Ma, with A-type granite and syenite emplaced in the eastern MLYRB at ca. 126 Ma and weak magmatic-hydrothermal activity in the western MLYRB at ca. 122–118 Ma.

In summary, the two types of Fe deposit not only share similar alteration assemblages and incursion of the evaporites within the ore-forming systems, but also may have been formed during corresponding magmatic-hydrothermal events. The Fe skarn deposits in the western part of the MLYRB are comparable to the magnetite-apatite deposits in the Cretaceous basins in the eastern part of the MLYRB, suggesting that they may appear in the same district and may have been formed during the same magmatic-hydrothermal events. This feature has been confirmed by research on the Longqiao Fe skarn deposit, located along the northern margin of the Luzong basin and with a formation age of ~130 Ma (Zhou et al., 2011b), and by recent exploration along the southern margin of the Ningwu basin, where magnetite-apatite deposits are highly-endowed (Lin and Xu, 2010; Li et al., 2014b). It is also proven by the discovery of magnetite-apatite ores in Wangbaoshan deposit located along the northeastern side of the Jinniu basin (near the Jinshandian pluton, Fig. 2a, b). These unique features are different from those of Fe skarn deposits in most global magnetite-apatite districts, such as Kiruna in northern Sweden (Sillitoe, 2003; Martinsson, 2004; Weihed et al., 2005; Groves et al., 2010), where Fe skarn and magnetite-apatite deposits were formed by different magmatic-hydrothermal events and have different formation ages.

6. Conclusions

1. The robustness of LA-MC-ICP-MS U–Pb zircon ages demonstrates that the quartz monzonite and quartz diorite of the Jinshandian intrusion were emplaced at ca. 130 Ma and 127 Ma, respectively. Ages of hydrothermal minerals (titanite and phlogopite) measured in this study indicate that the deposits within the Jinshandian ore field formed ca. 131–128 Ma, which is in excellent agreement with the ages of the Jinshandian intrusion. These data confirm a genetic link between the Jinshandian pluton and the surrounding Fe skarn mineralization.
2. The ages of hydrothermal minerals also indicate that at least two hydrothermal events have occurred within the Jinshandian Fe skarn ore field and they are separated by ca. ~10 m.y. The first event, responsible for the economic mineral deposits, ranges between 131 and 128 Ma, and the second, so far lacking any economic mineralization, is ~118 Ma. Integrating these ages with previous geochronological data, two distinct magmatic-hydrothermal events separated by ca ~10 m.y. characterize the entire Edong district after 135 Ma.
3. Detailed comparison of Fe skarn deposits in the western part of the MLYRB with magnetite-apatite deposits in the eastern part of the MLYRB suggests that these two types of deposit share many geological features, and may appear in the same district and form during the same magmatic-hydrothermal event.

Acknowledgements

We are very grateful to Bingfei Yu from the Central South Geo-Exploration Institute, and Weijin Ba and Ping Zhang from the Jinshandian Iron Deposit of the Wuhan Iron and Steel (Group) Corporation for their help during the field work. We would also like to thank Yueheng Yang for his assistance with the LA-ICP-MS U–Pb analyses of titanite. We also thank Prof. Richard Goldfarb for polishing the manuscript. This study was funded by the National Basic Research Program of China (973 Program) (2012CB416802), the National Special Research Programs for Non-Profit Trades (sponsored by MLR, 201311136), the Basic Scientific Research Operation Cost of State-Leveled Public Welfare Scientific Research Courtyard (K1203), and the Open Fund of MRL Key Laboratory of Metallogeny and Mineral Assessment, Institute of Mineral Resources, Chinese Academy of Geological Sciences (ZS1403).

References

Braxton, D.P., Cooke, D.R., Dunlap, J., Norman, M., Reiners, P., Stein, H., Waters, P., 2012. From crucible to graben in 2.3 Ma: a high-resolution geochronological study of porphyry life cycles, Boyongan-Bayugo copper-gold deposits, Philippines. Geology 40 (5), 471–474.

Cannell, J., Cooke, D.R., Walshe, J.L., Stein, H., 2005. Geology, mineralization, alteration, and structural evolution of the El Teniente porphyry Cu-Mo deposit. Econ. Geol. 100 (5), 979–1003.

Chang, Y.F., Liu, X.P., Wu, Y.C., 1991. The Copper-iron Belt of the Lower and Middle Reaches of the Changjiang River (in Chinese with English Abstract). Geological Publishing House, Beijing, pp. 1–234 (in Chinese with English abstract).

Chelle-Michou, C., Chiaradia, M., Béguelin, P., Ulianov, A., 2015. Petrological evolution of the magmatic suite associated with the Coroccohuayco Cu(–Au–Fe) porphyry–skarn deposit, Peru. J. Petrol. 56 (9), 1829–1862.

Chen, Z.H., Xing, G.F., Guo, K.Y., Zeng, Y., Kuang, F.X., He, Z.Y., Ke, X., Yu, M.G., Zhao, X.L., Zhang, Y., 2011. Zircon U-Pb ages of ore-bearing granitic bodies in northern Jiujiang-Ruichang metallogenic district of the mineralization belt of the Middle-Lower Reaches of the Yangtze River, and its geological significance. Acta Geol. Sin. 85 (7), 1146–1158 (in Chinese with English abstract).

Chiaradia, M., Schaltegger, U., Spikings, R., Wotzlaw, J.F., Ovtcharova, M., 2013. How accurately can we date the duration of magmatic-hydrothermal events in porphyry systems—an invited paper. Econ. Geol. 108 (4), 565–584.

Deckart, K., Clark, A.H., Celso, A.A., Ricardo, V.R., Bertens, A.N., Mortensen, J.K., Fanning, M., 2005. Magmatic and hydrothermal chronology of the giant Rio Blanco porphyry copper deposit, central Chile: implications of an integrated U-Pb and $^{40}Ar/^{39}Ar$ database. Econ. Geol. 100 (5), 905–934.

Deckart, K., Silva, W., Spröhnle, C., Vela, I., 2014. Timing and duration of hydrothermal activity at the Los Bronces porphyry cluster: an update. Mineral. Deposita 49 (5), 535–546.

Duan, C., Li, Y.H., Hou, K.J., Yuan, S.D., Liu, J.L., Zhang, C., 2012. Late Mesozoic ore-forming events in the Ningwu ore district, Middle-Lower Yangtze River polymetallic ore belt, east China: evidence from zircon U-Pb geochronology and Hf isotopic compositions of the granodioritic stocks. Acta Geol. Sin. Engl. 86 (3), 719–736.

Fan, H.Y., Li, W.D., Wang, W.B., 1995. On the relationship between the marine Triassic evaporite horizons and Cu(Au), Fe deposit in the Middle-Lower Yangtze area. Volcanol. Mineral Resour. 16 (2), 32–41 (in Chinese with English abstract).

Fan, Y., Zhou, T.F., Yuan, F., Qian, C.C., Lu, S.M., David, C., 2008. LAICP MS zircon U-Pb ages of the A-type granits in the Lu-Zong (Lujiang-Zongyang) area and their significances. Acta Petrol. Sin. 24 (8), 1715–1724 (in Chinese with English abstract).

Fan, Y., Zhou, T.F., Yuan, F., Zhang, L.J., Qian, B., Ma, L., Xie, J., Yang, X.F., 2011. Geochronology of the porphyry-like type iron deposits in Ning-Wu basin: evidence from $^{40}Ar–^{39}Ar$ phlogopite dating. Acta Geol. Sin. 85 (5), 810–820 (in Chinese with English abstract).

Fan, Y., Liu, Y.N., Zhou, T.F., Zhang, L.J., Yuan, F., Wang, W.C., 2014. Geochronology of the Nihe deposit and in the Lu-Zong basin and its metallogenic significances. Acta Petrol. Sin. 30 (5), 1369–1381 (in Chinese with English abstract).

Griffin, W., Powell, W., Pearson, N., O'Reilly, S., 2008. GLITTER: Data Reduction Software for Laser Ablation ICP-MS. Laser Ablation-ICP-MS in the Earth Sciences Mineralogical Association of Canada Short Course Series, vol. 40, pp. 204–207.

Groves, D.I., Bierlein, F.P., Meinert, L.D., Hitzman, M.W., 2010. Iron oxide copper-gold (IOCG) deposits through earth history: implications for origin, lithospheric setting, and distinction from other epigenetic iron oxide deposits. Econ. Geol. 105 (3), 641–654.

Hayden, L.A., Watson, E.B., Wark, D.A., 2008. A thermobarometer for sphene (titanite). Contrib. Mineral. Petrol. 155 (4), 529–540.

Hoskin, P., Black, L., 2000. Metamorphic zircon formation by solid-state recrystallization of protolith igneous zircon. J. Metamorph. Geol. 18 (4), 423–439.

Hou, K.J., Li, Y.H., Zou, T.R., Qu, X.M., Shi, Y.R., Xie, G.Q., 2007. Laser ablation-MC-ICP-MS technique for Hf isotope microanalysis of zircon and its geological applications. Acta Petrol. Sin. 23 (10), 2595–2604.

Hou, K.J., Yuan, S.D., 2010. Zircon U-Pb age and Hf isotopic composition of the volcanic and sub-volcanic rocks in the Ningwu basin and their geological implications. Acta Petrol. Sin. 26 (3), 888–902.

Hu, H., Lentz, D., Li, J.W., McCarron, T., Zhao, X.F., Hall, D., 2015. Reequlibration processes in magnetite from iron skarn deposits. Econ. Geol. 110 (1), 1–8.

Huang, G.C., Xia, J.L., Ding, L.X., Jin, S.G., Ke, Y.F., Wu, C.X., Zhu, J.M., 2013. Stage division and origin of Tonglushan pluton in southeast Hubei evidence from zircon U-Pb ages and Hf isotopes. Geol. China 40 (5), 1392–1408.

Kuiper, Y.D., 2002. The interpretation of inverse isochron diagrams in $^{40}Ar/^{39}Ar$ geochronology. Earth Planet. Sci. Lett. 203 (1), 499–506.

Li, J.W., Zhao, X.F., Zhou, M.F., Ma, C.Q., Souza, Z.S., Vasconcelos, P., 2009. Late Mesozoic magmatism from the Daye region, eastern China: U-Pb ages, petrogenesis, and geodynamic implications. Contrib. Mineral. Petrol. 157 (3), 383–409.

Li, J.W., Deng, X.D., Zhou, M.F., Liu, Y.S., Zhao, X.F., Guo, J.L., 2010. Laser ablation ICP-MS titanite U-Th–Pb dating of hydrothermal ore deposits: a case study of the Tonglushan Cu–Fe–Au skarn deposit, SE Hubei province, China. Chem. Geol. 270 (1), 56–67.

Li, J.W., Vasconcelos, P.M., Zhou, M.F., Deng, X.D., Cohen, B., Bi, S.J., Zhao, X.F., Selby, D., 2014a. Longevity of magmatic–hydrothermal systems in the Daye Cu–Fe–Au District, eastern China with implications for mineral exploration. Ore Geol. Rev. 57, 375–392.

Li, R.L., Zhu, Q.Q., Hou, K.J., Xie, G.Q., 2012. Zircon U-Pb dating and Hf isotopic compositions of granite porphyry and rhyolite porphyry from Jingniu basin in the Middle-Lower Yangtze River Belt and its geological significance. Acta Petrol. Sin. 28 (10), 3347–3360 (in Chinese with English abstract).

Li, W., Xie, G.Q., Zhu, Q.Q., Zheng, X.W., Zhang, Z.Y., Han, Y.X., 2016. Multi-superimposed mineralization process in Chengchao iron deposit, southeastern Hubei Province: evidence from the study of magnetite. Acta Petrol. Sin. 32 (2), 471–492 (in Chinese with English abstract).

Li, W.T., Audétat, A., Zhang, J., 2015. The role of evaporites in the formation of magnetite–apatite deposits along the Middle and Lower Yangtze River, China: evidence from LA-ICP-MS analysis of fluid inclusions. Ore Geol. Rev. 67, 264–278.

Li, Y.H., Duan, C., Han, D., Chen, X.W., Wang, C.L., Yang, B.Y., Zhang, C., Liu, F., 2014b. Effect of sulfate evaporate salt layer for formation of porphyrite iron ores in the Middle-Lower Yangtze River area. Acta Geol. Sin. 30 (5), 1355–1368 (in Chinese with English abstract).

Lin, G., Xu, D.R., 2010. Prospecting for Daye-type iron deposit in depth of porphyrite-type iron deposit: a case study of southern Ningwu iron deposits in Anhui province. Mineral Deposits 29 (3), 427–436 (in Chinese with English abstract).

Liu, Y.S., Hu, Z.C., Zong, K.Q., Gao, C.G., Gao, S., Xu, J., Chen, H.H., 2010. Reappraisement and refinement of zircon U-Pb isotope and trace element analyses by LA-ICP-MS. Chin. Sci. Bull. 55 (15), 1535–1546.

Ludwig, K.R., 2003. ISOPLOT 3.00: A Geochronological Toolkit for Microsoft Excel. Berkeley Geochronology Center, California, Berkeley.

Ma, F., Jiang, S.Y., Xue, H.M., 2010. Early Cretaceous mineralizations Ningwu basin: insight from actinolite $^{39}Ar–^{40}Ar$ laser dating results. Mineral Deposits 29 (2), 283–289 (in Chinese with English abstract).

Maksaev, V., Munizaga, F., McWilliams, M., Fanning, M., Mathur, R., Ruiz, J., Zentilli, M., 2004. New chronology for El Teniente, Chilean Andes, from U/Pb, $^{40}Ar/^{39}Ar$, Re/Os and fission-track dating: implications for the evolution of a supergiant porphyry Cu-Mo deposit. In: Sillitoe, R.H., Perelló, J. (Eds.), Andean Metallogeny: New Discoveries, Concepts and Updates. Society of Economic Geologists, pp. 15–54.

Mao, J.W., Wang, Y.T., Lehmann, B., Yu, J.J., Du, A.A., Mei, Y.X., Li, Y.F., Zang, W.S., Stein, H.J., Zhou, T.F., 2006. Molybdenite Re–Os and albite $^{40}Ar/^{39}Ar$ dating of Cu–Au–Mo and magnetite porphyry systems in the Yangtze River valley and metallogenic implications. Ore Geol. Rev. 29, 307–324.

Mao, J.W., Xie, G.Q., Duan, C., Pirajno, F., Ishiyama, D., Chen, Y.C., 2011. A tectono-genetic model for porphyry–skarn–stratabound Cu–Au–Mo–Fe and magnetite–apatite deposits along the Middle-Lower Yangtze River Valley, Eastern China. Ore Geol. Rev. 43, 294–314.

Mao, J.W., Duan, C., Liu, J.L., Zhang, C., 2012. Metallogeny and corresponding mineral deposit model of the Cretaceous terrestrial volcanic-intrusive rocks-related polymetallic iron deposits in Middle-Lower Yangtze River Valley. Acta Petrol. Sin. 28 (1), 1–14 (in Chinese with English abstract).

Martinsson, O., 2004. Metallogeny of the northern Norrbotten Fe-Cu-Au-ore province. In: Allen, R., Martinsson, O., Weihed, P. (Eds.), Svecofennian Ore-Forming Environments Field Trip Volcanic-associated Zn-Cu-Au-Ag and Magnetite-apatite, Sediment-hosted Pb-Zn, and Intrusion-associated Cu-Au Deposits in Northern Sweden. Society of Economic Geologists, pp. 26–28.

McDougall, I., Harrison, T., 1999. Geochronology and Thermochronology by the $^{40}Ar/^{39}Ar$ Method. Oxford University Press, Oxford, UK, p. 269.

Meinert, L.D., Dipple, G.M., Nicolescu, S., 2005. World skarn deposits. Econ. Geol. 100th Anniversary, pp. 299–336.

Ningwu Research Group, 1978. The Porphyrite Iron Deposit of Ningwu. Geological Publishing House, Beijing, pp. 1–196 (in Chinese).

Pan, Y.M., Dong, P., 1999. The Lower Changjiang (Yangzi/Yangtze River) metallogenic belt, east central China: intrusion- and wall rock-hosted Cu–Fe–Au, Mo, Zn, Pb, Ag deposits. Ore Geol. Rev. 15, 177–242.

Pirajno, F., Zhou, T.F., 2015. Intracontinental porphyry and porphyry–skarn mineral systems in eastern China: scrutiny of a special case "Made-in-China". Econ. Geol. 110 (3), 603–629.

Qu, H.Y., Wang, H.L., Pei, R.F., Yao, L., Wang, Y.L., Zheng, Z.G., 2012. Zircon U-Pb geochronological and Hf isotopic constraints on petrogenesis of Tieshan and Jinshandian plutons in the southeastern Hubei Province. Acta Petrol. Sin. 28 (1), 147–165.

Shu, Q.A., Chen, P.L., Cheng, J.R., 1992. Geology of Fe-Cu Ore Deposits in Eastern Hubei Province (in Chinese with English abstract). Press of Metallurgical Industry, Beijing, pp. 1–510 (in Chinese with English abstract).

Sillitoe, R.H., 2003. Iron oxide-copper-gold deposits: an Andean view. Mineral. Deposita 38 (7), 787–812.

Sillitoe, R.H., Mortensen, J.K., 2010. Longevity of porphyry copper formation at Guellaveco, Peru. Econ. Geol. 105 (6), 1157–1162.

Spencer, E.T., Wilkinson, J.J., Creaser, R.A., Seguel, J., 2015. The distribution and timing of molybdenite mineralization at the El Teniente Cu–Mo porphyry deposit, Chile. Econ. Geol. 110 (2), 387–421.

Spencer, K.J., Hacker, B.R., Kylander-Clark, A.R.C., Andersen, T.B., Cottle, J.M., Stearns, M.A., Poletti, J.E., Seward, G.G.E., 2013. Campaign-style titanite U-Pb dating by laser-ablation ICP: implications for crustal flow, phase transformations and titanite closure. Chem. Geol. 341, 84–101.

Stacey, J.S., Kramers, J.D., 1975. Approximation of terrestrial lead isotope evolution by a two-stage model. Earth Planet. Sci. Lett. 26 (2), 207–221.

Steiger, R.H., Jäger, E., 1977. Subcommission on geochronology: convention on the use of decay constants in geo-and cosmochronology. Earth Planet. Sci. Lett. 36 (3), 359–362.

Stein, H.J., Cathles, L.M., 1997. Preface. A special issue on the timing and duration of hydrothermal events. Econ. Geol. 92 (7), 763–765.

Sun, J.F., Yang, J.H., Wu, F.Y., Li, X.H., Yang, Y.H., Xie, L.W., Wilde, S.A., 2010. Magma mixing controlling the origin of the Early Cretaceous Fangshan granitic pluton, North China Craton: in situ U-Pb age and Sr–, Nd–, Hf– and O–isotope evidence. Lithos 120, 421–438.

Sun, J.F., Yang, J.H., Wu, F.Y., Xie, L.W., Yang, Y.H., Liu, Z.C., Li, X.H., 2012. In situ U-Pb dating of titanite by LA-ICPMS. Chin. Sci. Bull. 57 (20), 2506–2516.

Von Quadt, A., Erni, M., Martinek, K., Moll, M., Peytcheva, I., Heinrich, C.A., 2011. Zircon crystallization and the lifetimes of ore-forming magmatic hydrothermal systems. Geology 39 (8), 731–734.

Vry, V.H., Wilkinson, J.J., Seguel, J., Millán, J., 2010. Multistage intrusion, brecciation, and veining at El Teniente, Chile: evolution of a nested porphyry system. Econ. Geol. 105 (1), 119–153.

Wang, G.D., Song, X., 1996. Multi-stage enrichment-the key mechanism for iron ore in China and discussion on rion ore prospecting in Middle and Lower Yangtze River. Contrib. Geol. Mineral Resour. Res. 11 (1), 1–7 (in Chinese with English abstract).

Wang, L.J., Wang, R.C., Yu, J.H., Yang, Y.H., Huang, J.P., Zhang, S.Q., 2014. Geochronology, geochemistry of volcanic-intrusive rocks in the Ningwu basin and its geological implications. Acta Geol. Sin. 88 (7), 1247–1272 (in Chinese with English abstract).

Wang, S.S., 1983. Age determinations of ^{40}Ar–^{40}K, ^{40}Ar–^{39}Ar and radiogenic ^{40}Ar released characteristics on K-Ar geostandards of China. Sci. Geol. Sin. 4, 315–323.

Wang, S.W., Zhou, T.F., Yuan, F., Fan, Y., Cooke, D.R., Zhang, L.J., Fu, B., White, N.C., 2016. Geochemical characteristics of the Shujiadian Cu deposit related intrusion in Tongling: petrogenesis and implications for the formation of porphyry Cu systems in the Middle-Lower Yangtze River Valley metallogenic belt, eastern China. Lithos 252–253, 185–199.

Weihed, P., Arndt, N., Billström, K., Duchesne, J.-C., Eilu, P., Martinsson, O., Papunen, H., Lahtinen, R., 2005. 8: Precambrian geodynamics and ore formation: the Fennoscandian shield. Ore Geol. Rev. 27, 273–322.

Xie, G.Q., Mao, J.W., Li, R.L., Zhou, S.D., Ye, H.S., Yan, Q.R., Zhang, Z.S., 2006. SHRIMP zircon U-Pb dating for volcanic rocks of the Dasi Formation in southeast Hubei province, middle–lower reaches of the Yangtze River and its implications. Chin. Sci. Bull. 51 (24), 3000–3009.

Xie, G.Q., Mao, J.W., 2008. Zircon SHRIMP U-Pb dating of Echeng granite in the southeastern Hubei MLYB, Eastern China. Geochim. Cosmochim. Acta 72 (12), A1042.

Xie, G.Q., Mao, J.W., Li, R.L., Bierlein, F.P., 2008. Geochemistry and Nd–Sr isotopic studies of Late Mesozoic granitoids in the southeastern Hubei Province, Middle-Lower Yangtze River belt, Eastern China: petrogenesis and tectonic setting. Lithos 104, 216–230.

Xie, G.Q., Mao, J.W., Li, X.W., Duan, C., Yao, L., 2011a. Late Mesozoic bimodal volcanic rocks in the Jinniu basin, Middle-Lower Yangtze River Belt (YRB), East China: age, petrogenesis and tectonic implications. Lithos 127, 144–164.

Xie, G.Q., Mao, J.W., Zhao, H.J., 2011b. Zircon U-Pb geochronological and Hf isotopic constraints on petrogenesis of Late Mesozoic intrusions in the southeast Hubei Province, Middle-Lower Yangtze River belt (MLYRB), East China. Lithos 125, 693–710.

Xie, G.Q., Mao, J.W., Zhao, H.J., Wei, K.T., Jin, S.G., Pan, H.J., Ke, Y.Y., 2011c. Timing of skarn deposit formation of the Tonglushan ore district, southeastern Hubei Province, Middle-Lower Yangtze River Valley metallogenic belt and its implications. Ore Geol. Rev. 43, 62–77.

Xie, G.Q., Mao, J.W., Zhao, H.J., Duan, C., Yao, L., 2012. Zircon U-Pb and phlogopite ^{40}Ar–^{39}Ar age of the Chengchao and Jinshandian skarn Fe deposits, southeast Hubei Province, Middle-Lower Yangtze River Valley metallogenic belt, China. Mineral. Deposita 47 (6), 633–652.

Xie, G.Q., Zhu, Q.Q., Yao, L., Wang, J., Li, W., 2013. Discussion on regional metal mineral deposit model of Late Mesozoic Cu–Fe–Au polymetallic deposits in the Southeast Hubei Province. Bull. Mineralo. Petrol. Geochem. 32 (4), 418–426 (in Chinese with English abstract).

Xie, G.Q., Mao, J.W., Zhu, Q.Q., Yao, L., Li, Y.H., Li, W., Zhao, H.J., 2015. Geochemical constraints on Cu–Fe and Fe skarn deposits in the Edong district, Middle-Lower Yangtze River metallogenic belt, China. Ore Geol. Rev. 64, 425–444.

Yan, J., Liu, H.Q., Song, C.Z., Xu, X.S., An, Y.J., Liu, J., Dai, L.Q., 2009. Zircon U-Pb geochronology of the volcanic rocks from Fanchang-Ningwu volcanic basins in the Lower Yangtze region and its geological implications. Chin. Sci. Bull. 54 (16), 2895–2904.

Yan, J., Peng, G., Liu, J.M., Li, Q.Z., Chen, Z.H., Shi, L., Liu, X.Q., Jiang, Z.Z., 2012. Petrogenesis of granites from Fanchang district, the Lower Yangtze region: zircon geochronology and Hf–O isotopes constrains. Acta Petrol. Sin. 28 (10), 3209–3227 (in Chinese with English abstract).

Yang, Y.H., Wu, F.Y., Wilde, S.A., Liu, X.M., Zhang, Y.B., Xie, L.W., Yang, J.H., 2009. In situ perovskite Sr–Nd isotopic constraints on the petrogenesis of the Ordovician Mengyin kimberlites in the North China Craton. Chem. Geol. 264 (1), 24–42.

Yao, L., Xie, G., Mao, J., Lü, Z., Zhao, C., Zheng, X., Ding, N., 2015. Geological, geochronological, and mineralogical constraints on the genesis of the Chengchao skarn Fe deposit, Edong ore district, Middle-Lower Yangtze River Valley metallogenic belt, eastern China. J. Asian Earth Sci. 101, 68–82.

Yao, P.H., Wang, K.N., Du, C.L., Lin, Z.T., Song, X., 1993. Records of China's Iron Ore Deposits. Metallurgic Industry, Beijing, pp. 1–662 (in Chinese).

Yuan, F., Zhou, T.F., Fan, Y., Huang, Y.M., Zhang, L.J., 2010a. LA-ICPMS U-Pb ages of zircons from Mesozoic volcanic rocks and their significance in Fanchang basin, Anhui Province, China. Acta Petrol. Sin. 26 (9), 2805–2817.

Yuan, S.D., Hou, K.J., Liu, M., 2010b. Timing of mineralization and geodynamic framework of iron-oxide-apatite deposits in Ningwu Cretaceous basin in the Middle-Lower Reaches of the Yangtze River, China: constraints from Ar–Ar dating on phlogopites. Acta Petrol. Sin. 26 (3), 797–808 (in Chinese with English abstract).

Zhai, Y.S., Xiong, Y.I., Yao, S.Z., Lin, X.D., 1996. Metallogeny of copper and iron deposits in the Eastern Yangtse Craton, east-central China. Ore Geol. Rev. 11, 229–248.

Zhang, Q., Jian, P., Liu, D.Y., Wang, Y.L., Qian, Q., Wang, Y., Xue, H.M., 2003. SHRIMP dating of volcanic rocks from Ningwu area and its geological implications. Sci. China Ser. D 46 (8), 830–837.

Zhang, R.H., 1986. Sulfur isotopes and pyrite-anhydrite equilibria in a volcanic basin hydrothermal system of the Middle-Lower Yangtze River valley. Econ. Geol. 81 (1), 32–45.

Zhang, Z.C., Hou, T., Santosh, M., Li, H.M., Li, J.W., Zhang, Z.H., Song, X.Y., Wang, M., 2014. Spatio-temporal distribution and tectonic settings of the major iron deposits in China: an overview. Ore Geol. Rev. 57, 247–263.

Zhang, Z.C., Santosh, M., Li, J.W., 2015b. Iron deposits in relation to magmatism in China. J. Asian Earth Sci. 113, 951–956.

Zhao, Y.M., Lin, W.W., Bi, C.S., Li, D.X., Jiang, C.J., 1990. Skarn deposits of China (in Chinese with English abstract). Geology Press, Beijing, pp. 1–354 (in Chinese with English abstract).

Zhou, T.F., Fan, Y., Yuan, F., 2008a. Advances on petrogensis and metallogeny study of the mineralization belt of the Middle and Lower Reaches of the Yangtze River area. Acta Petrol. Sin. 24 (8), 1665–1678 (in Chinese with English abstract).

Zhou, T.F., Fan, Y., Yuan, F., Lu, S.M., Shang, S.G., Cooke, D.R., Meffre, S., Zhao, G.C., 2008b. Geochronology of the volcanic rocks in the Lu-Zong basin and its significance. Sci. China Ser. D 51 (10), 1470–1482.

Zhou, T.F., Fan, Y., Yuan, F., Zhang, L.J., Qian, C.C., Lu, S.M., Cooke, D.R., 2010. Temporal-spatial framework of magmatic intrusions in Luzong volcanic basin in East China and their constrain to mineralizations. Acta Petrol. Sin. 26 (9), 2694–2714 (in Chinese with English abstract).

Zhou, T.F., Fan, Y., Yuan, F., Zhang, L.J., Ma, L., Qian, B., Xie, J., 2011a. Petrogensis and metallogeny study of the volcanic basins in the Middle and Lower Yangtze metallogenic belt. Acta Geol. Sin. 85 (5), 712–730 (in Chinese with English abstract).

Zhou, T.F., Wu, M.G., Fan, Y., Duan, C., Yuan, F., Zhang, L.L., Liu, J., Qian, B., Pirajno, F., Cooke, D.R., 2011b. Geological, geochemical characteristics and isotope systematics of the Longqiao iron deposit in the Lu-Zong volcano-sedimentary basin, Middle-Lower Yangtze (Changjiang) River Valley, Eastern China. Ore Geol. Rev. 43, 154–169.

Zhou, T.F., Wang, B., Fan, Y., Yuan, F., Zhang, L.J., Zhong, G.X., 2012. Apatite-actinolite-magnetite deposit related to A-tpye granite in Luzong basin: evidence from Makou iron deposit. Acta Petrol. Sin. 28 (10), 3087–3098 (in Chinese with English abstract).

Zhou, T.F., Fan, Y., Yuan, F., Wu, M.A., Zhao, W.G., Qian, B., Ma, L., Wang, W.C., Liu, Y. N., Noel, W., 2014. The metallogenic model of Nihe iron deposit in Luzong basin and genetic relationship between gypsum-salt layer and deposit. Acta Geol. Sin. 88 (4), 562–573 (in Chinese with English abstract).

Zhou, T.F., Wang, S.W., Yuan, F., Fan, Y., Zhang, D.Y., Chang, Y.F., White, N.C., 2016. Magmatism and related mineralization of the intracontinental porphyry deposits in the Middle-Lower Yangtze River Valley Metallogenic Belt. Acta Petrol. Sin. 32 (2), 271–288 (in Chinese with English abstract).

Zhu, Q.Q., Xie, G.Q., Mao, J.W., Li, W., Li, Y.H., Wang, J., Zhang, P., 2015. Mineralogical and sulfur isotopic evidence for the incursion of evaporites in the Jinshandian skarn Fe deposit, Edong district, Eastern China. J. Asian Earth Sci. 113, 1253–1267.